

CarbonTracker Documentation

CT2015 release

CarbonTracker Team

March 17, 2016

Contents

1	Introduction	1
1.1	A tool for science, and policy	1
1.2	A community effort	2
1.3	Updates	2
1.4	The role of other atmospheric species in constraining the atmospheric carbon budget	3
2	Terrestrial biosphere module	3
2.1	CASA model	4
2.2	Temporal downscaling	5
2.2.1	Smooth month-to-month variations	6
2.3	GFED4.1s and GFED_CMS	7
2.4	References	8
3	Fire module	10
3.1	Global Fire Emissions Database (GFED)	10
3.2	Fire Inventory from NCAR (FINN)	11
3.3	References	11
4	Fossil fuel module	13

4.1	The “Miller” emissions dataset	14
4.2	The “ODIAC” emissions dataset	15
4.3	Uncertainties	16
4.4	References	18
5	Oceans module	19
5.1	Air-sea gas exchange	21
5.2	OIF: the Ocean Inversion Fluxes prior	21
5.3	$p\text{CO}_2\text{-Clim}$: Takahashi <i>et al.</i> (2009) climatology prior	22
5.4	Gas-transfer velocity and ocean surface properties	22
5.5	Specifics of the inversion methodology related to air-sea CO_2 fluxes	23
5.6	References	24
6	Atmospheric transport	26
6.1	TM5 offline tracer transport model	26
6.2	Convective flux fix	28
6.3	References	30
7	Observations	31
7.1	The CarbonTracker observational network	31
7.2	Adaptive model-data mismatch	35
7.3	Statistical performance of CT2015	36
7.4	References	45
8	Ensemble data assimilation	45
8.1	Parameterization of unknowns	46
8.1.1	Optimization regions	46
8.1.2	Ensemble size and localization	48
8.1.3	Dynamical model	48
8.2	Covariance structure	49
8.3	Multiple prior models	50
8.3.1	Posterior uncertainties in CarbonTracker	50

8.4	References	52
9	Ecoregions in CarbonTracker	52
9.1	What are ecoregions?	52
9.2	Why use ecoregions?	54
9.3	Ecosystems within TransCom regions	54
9.4	References	54

1 Introduction

The goal of the CarbonTracker program is to produce quantitative estimates of atmospheric carbon uptake and release for North America and the rest of the world that are consistent with observed patterns of CO₂ in the atmosphere.

1.1 A tool for science, and policy

CarbonTracker and the associated long-term monitoring of atmospheric CO₂ helps improve our understanding of how carbon uptake and release from land ecosystems and oceans are responding to a changing climate, increasing levels of atmospheric CO₂ (higher CO₂ may enhance plant growth) and other environmental changes, including human management of land and oceans. The open access to all CarbonTracker results means that anyone can scrutinize our work, suggest improvements, and profit from our efforts. This will accelerate the development of a tool that can monitor, diagnose, and possibly predict the behavior of the global carbon cycle, and the climate that is so intricately connected to it.

CarbonTracker can become a policy support tool too. Its ability to accurately quantify natural and anthropogenic emissions and uptake at regional scales is currently limited by a sparse observational network. With enough observations, it will become possible to keep track of regional emissions, including those from fossil fuel use, over long periods of time. This will provide an independent check on emissions accounting, estimates of fossil fuel use based on economic inventories. It can thus provide feedback to policies aimed at limiting greenhouse gas emissions. This independent measure of effectiveness of any policy, provided by the atmosphere itself (where CO₂ levels matter most), is the bottom line in any mitigation strategy.

1.2 A community effort

CarbonTracker is intended to be a tool for the community and we welcome feedback and collaboration from anyone interested. Our ability to accurately track carbon with more spatial and temporal detail is dependent on our collective ability to make enough measurements and to obtain enough air samples to characterize variability present in the atmosphere. For example, estimates suggest that observations from tall communication towers (taller than 200m) can tell us about carbon uptake and emission over a radius of only several hundred kilometers. The [map of observation sites](#) shows how sparse the current network is. One way to join this effort is by contributing measurements. Regular air samples collected from the surface, towers or aircraft are needed. It would also be very fruitful to expand use of continuous measurements like the ones now being made on very tall (more than 200m) communications towers. Another way to join this effort is by volunteering flux estimates from your own work, to be run through CarbonTracker and assessed against atmospheric CO₂. Please [contact us](#) if you would like to get involved and collaborate with us.

1.3 Updates

CarbonTracker is updated about once per year to include new data and model improvements. The updated calculations are produced for the year 2000 through the most recent complete year of observations. Previous versions are available at [the CarbonTracker website](#), and the effect of significant changes to any of the system components is noted.

Important revisions of our methods for CT2015 include the following:

- Use of “adaptive” model-data mismatch scheme.
- Use of hourly data at continuous measurement sites.
- New land and wildfire priors

1.4 The role of other atmospheric species in constraining the atmospheric carbon budget

Many laboratories making high accuracy CO₂ observations also make many other measurements of the same air, typically other greenhouse gases such as methane CH₄, nitrous oxide N₂O, sulfur hexafluoride SF₆, as well as carbon monoxide (CO) and isotopic ratios of CO₂ and CH₄. These measurements are usually made as mole fractions, for reasons explained here.

These trace gases are relevant for climate change and interesting in their own right, but the additional measurements can also help in source identification or process understanding. For this reason a series of halocompounds and hydrocarbons have recently been added to the analysis of a subset of air samples. Several of these species can be useful for monitoring air quality, but they can also help with better source apportionment of the greenhouse gases. In addition, the estimation of the source strengths of a number of pollutants could be greatly improved if we were able to quantify fossil fuel CO₂ emissions from air measurements for specified regions.

The best tracer for quantifying the component of atmospheric CO₂ that has been recently added to an air mass through the burning of fossil fuels is the decrease of the carbon-14 content of CO₂. Cosmic rays produce carbon-14, a radioactive form of carbon, in the higher regions of the atmosphere. It is present in the atmosphere and oceans and in all living organisms and their remains, but coal, oil, and natural gas contain no carbon-14 because it has long decayed away. Currently, carbon-14 measurements are made on only a small subset of the air samples because of higher analysis costs. None of these other data and their relationships have been used in this release of CarbonTracker. We expect them to be incorporated gradually at later stages.

CarbonTracker is a NOAA contribution to the [North American Carbon Program](#).

2 Terrestrial biosphere module

The biospheric component of the terrestrial carbon cycle consists of all the carbon stored in ‘biomass’ around us. This includes trees, shrubs, grasses, carbon within soils, dead wood, and leaf litter. Such reservoirs of carbon can exchange CO₂ with the atmosphere. Exchange starts when plants take up CO₂ during their growing season through the process called photosynthesis (uptake). Most of this carbon is released back to the atmosphere throughout the year through a process called respiration (release). This includes both the decay of dead wood and litter and the metabolic respiration of living plants. Of course, plants can also return carbon to the atmosphere when they burn, as described in Section 3. Even though the yearly sum of uptake and release of carbon amounts to a relatively small number (a few petagrams (one Pg=10¹⁵ g)) of carbon per year, the flow of carbon each way is as large as 120 PgC each year. This is why the net result of these flows needs to be monitored in a system such as ours. It is also the reason we need a good physical description (model) of these flows of carbon. After all, from the atmospheric measurements we can only see the small net sum of the large two-way streams (gross fluxes). Information on what the biospheric fluxes are doing in

each season, and in every location on Earth is derived from a specialized biosphere model, and fed into our system as a first guess, to be refined by our assimilation procedure.

2.1 CASA model

Two biosphere models currently provide first-guess terrestrial fluxes for CT2015. Both models are versions of the Carnegie-Ames Stanford Approach (CASA) biogeochemical model introduced by Potter *et al.*(1993). CASA calculates global carbon fluxes using input from weather models to drive biophysical processes, and satellite observed Normalized Difference Vegetation Index (NDVI) to track plant phenology. The models are driven by year-specific weather and satellite observations, and include the effects of fires on photosynthesis and respiration (see van der Werf *et al.*, 2006, and Giglio *et al.*, 2006). Both simulations provide $0.5^\circ \times 0.5^\circ$ global fluxes with a monthly time resolution.

CASA models provide monthly-mean Net Primary Production (NPP) and heterotrophic respiration (R_H) for each terrestrial grid cell being simulated. NPP is the difference in photosynthetic carbon uptake (Gross Primary Production, GPP) and the carbon release by the same plants due to “maintenance respiration”, which is also called autotrophic respiration, R_A . The carbon uptake represented by NPP and carbon release represented by R_H can be differenced to provide Net Ecosystem Exchange (NEE) of CO_2 . Throughout this discussion, we use the convention that fluxes carry algebraic signs and we adopt the “atmospheric perspective” for those signs. Thus carbon uptake by the terrestrial biosphere is a negative flux to the atmosphere, and release of CO_2 back to the atmosphere is a positive flux. This means that we represent all respiration fluxes as positive and GPP as negative, so $\text{NEE} = \text{NPP} + R_H$. This stands in contrast to convention in the terrestrial carbon community, where all fluxes are generally non-negative.

2.2 Temporal downscaling

Use of monthly-mean terrestrial fluxes to simulate atmospheric CO_2 is not sufficient to resolve the variability observed at measurement sites. Instead, higher-frequency variations, including the diurnal cycle and effects of passing weather systems must be imposed on the CASA monthly fluxes. Following the logic laid out by Olsen and Randerson (2004), we transform the CASA-supplied monthly-mean NPP and R_H fluxes into GPP and total ecosystem respiration, $R_E = R_A + R_H$.

To estimate sub-monthly variations, including diurnal and synoptic variability, the Olsen and Randerson

(2004) strategy is to model GPP as a linear function of incoming surface solar radiation and total ecosystem respiration as a function of near-surface temperature.

The fundamental assumption needed to apply this scheme is that we can resolve CASA-simulated NPP into GPP and R_A . We apply the assumption that GPP is twice NPP, which further implies that R_A is the same size as NPP (but of opposite sign):

$$\text{GPP} = 2 * \text{NPP}, \quad (1)$$

$$\text{NPP} = \text{GPP} + R_A, \quad (2)$$

and

$$R_A = -1 * \text{NPP}. \quad (3)$$

We use meteorological fields from the European Centre for Medium-Range Weather Forecasts (ECMWF) ERA-interim reanalysis to supply temperature and shortwave radiation. Fluxes are generated with 90-minute variability using a simple temperature Q_{10} relationship for respiration, assuming a global Q_{10} value of 1.5, and a linear scaling of photosynthesis with solar radiation. The procedure is very similar, but **NOT** identical to the procedure in Olsen and Randerson (2004). Note that the introduction of 90-minute variability conserves the monthly mean NEE from the CASA model. Instantaneous NEE for each 90-minute interval is created as:

$$\text{NEE}(t) = \text{GPP}(t) + R_E(t), \quad (4)$$

where

$$\text{GPP}(t) = \text{GPP}_{\text{mean}}(I(t)/I_{\text{mean}}) \quad (5)$$

$$R_E(t) = R_{E,\text{mean}}(Q_{10}(t)/Q_{10,\text{mean}}), \quad (6)$$

and Q_{10} is computed as

$$Q_{10}(t) = 1.5^{(T_{2m}(t)-273.15)/10.0}, \quad (7)$$

where T_{2m} is 2 meter temperature in Kelvin, I is surface solar radiation, t is time in 90-minute intervals, and x_{mean} represents the monthly mean of quantity x , including monthly-mean fluxes derived from the CASA model.

2.2.1 Smooth month-to-month variations

While the scheme outlined above imposes realistic diurnal- and synoptic-scale variations on monthly-mean GPP and R_E , it still allows for abrupt changes from one month to the next. For CT2015, we add a further processing step designed to remove such unrealistic step changes. We fit smooth curves to the monthly GPP and R_E using the piecewise integral quadratic splines (PIQS) of Rasmussen (1991). These PIQS fits are continuous in the first and second derivatives, and have the property of preserving monthly mean flux. We use a similar scheme to smooth over year-to-year step changes in fossil fuel emissions. The final smoothed GPP is

$$\text{GPP}_F(t) = \text{GPP}(t) - \text{GPP}_{\text{mean}} + \text{GPP}_{\text{PIQS}}(t), \quad (8)$$

and the final smoothed ecosystem respiration is

$$R_{E,F}(t) = R_E(t) - R_{E,\text{mean}} + R_{E,\text{PIQS}}(t). \quad (9)$$

Together, these form the terrestrial NEE imposed as a first-guess flux in CT2015:

$$\text{NEE}_F(t) = \text{GPP}_F(t) + R_{E,F}(t). \quad (10)$$

2.3 GFED4.1s and GFED_CMS

CarbonTracker uses fluxes from CASA runs from two models associated with the GFED project as its first guess for terrestrial biosphere fluxes. We have found a significantly better match to observations when using this output compared to the fluxes from a neutral biosphere simulation. Both of the CASA simulations used in CT2015 (GFED 4.1s and GFED_CMS) are driven by [AVHRR NDVI](#). This satellite driver tends to

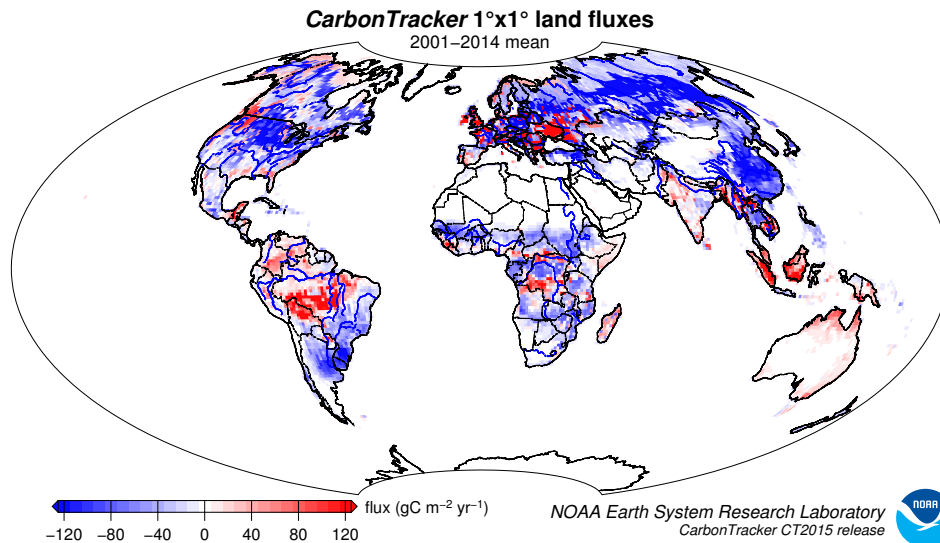


Figure 1: Map of optimized global biosphere fluxes. The pattern of net ecosystem exchange (NEE) of CO₂ of the land biosphere averaged over the time period indicated, as estimated by CarbonTracker. This NEE represents land-to-atmosphere carbon exchange from photosynthesis and respiration in terrestrial ecosystems, and a contribution from fires. It does not include fossil fuel emissions. Negative fluxes (blue colors) represent CO₂ uptake by the land biosphere, whereas positive fluxes (red colors) indicate regions in which the land biosphere is a net source of CO₂ to the atmosphere. Units are gC m⁻² yr⁻¹.

produce a larger-amplitude annual cycle of NEE compared to the alternative driver, [MODIS fPAR](#). As one of the robust results of atmospheric inversions is a deeper annual cycle of terrestrial NEE, inversions using NDVI-driven first-guess fluxes perform slightly better than those with a MODIS fPAR driver.

The record of atmospheric CO₂ calls for a deeper terrestrial biosphere sink than that generally simulated by forward models like CASA. This is manifested by a larger annual cycle of terrestrial biosphere fluxes, and in particular a deeper boreal summer uptake of carbon dioxide, in the posterior optimized fluxes compared to the prior models (See Fig. 2). We call upon the atmospheric CO₂ observations to make this change, and in order to handle these prior model differences the ensemble Kalman filter’s prior covariance model has been re-tuned. In short, this prior uncertainty needs to comfortably span differences among the terrestrial biosphere priors, the fossil fuel emissions priors, and adjustments to fluxes required to bring model predictions into agreement with observations. As a result, the land biosphere prior uncertainty is larger in CT2015 in comparison to previous releases. Details can be found in Section 8.

CarbonTracker CT2015 is a full reanalysis of the 2000-2014 period using new fossil fuel emissions, CASA-GFED v4.1s and FINN v1.5 fire emissions, and first-guess biosphere model fluxes derived from CASA-GFED v4.1s for 4 of our inversions, and from CASA GFED_CMS for the remaining 4 inversions.

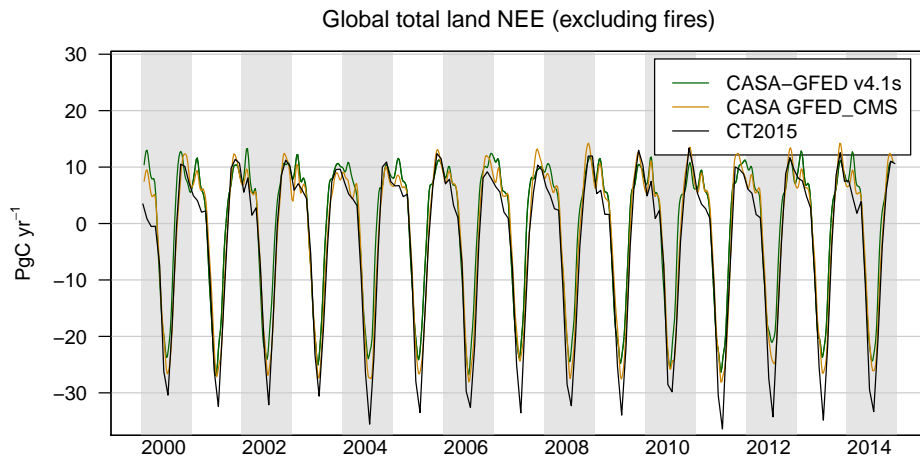


Figure 2: Time series of global-total terrestrial biosphere flux between the two priors and the CT2015 posterior. Global CO₂ uptake by the land biosphere, expressed in PgC yr⁻¹, excluding emissions by wildfire. Positive flux represents emission of CO₂ to the atmosphere, and the negative fluxes indicate times when the land biosphere is a sink of CO₂. Optimization against atmospheric CO₂ data requires a larger land sink than in either prior, which effectively requires a deeper annual cycle. This is shown by the CT2015 posterior (black).

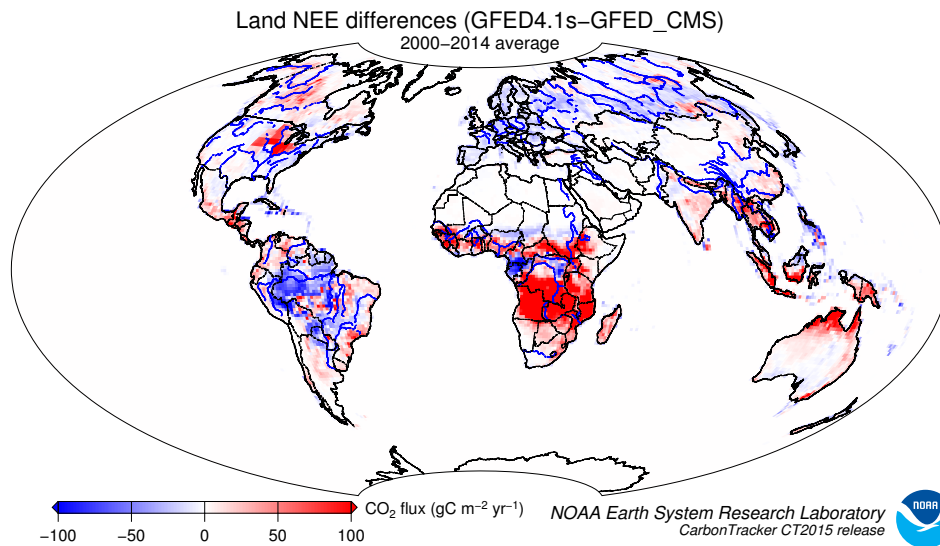


Figure 3: Differences in long-term mean terrestrial biosphere fluxes between the two priors. Red indicates areas where the GFED4.1s prior has less terrestrial uptake (or more outgassing to the atmosphere) than the GFED_CMS prior, and blue represents the opposite. Units are gC m⁻² yr⁻¹.

Due to the inclusion of fires, inter-annual variability in weather and NDVI, the fluxes for North America start with a small net flux even when no assimilation is done. This first-guess flux ranges from neutral exchange to about 0.5 PgC yr^{-1} of uptake.

2.4 References

- Potter, C. S., J. T. Randerson, C. B. Field, P. A. Matson, P. M. Vitousek, H. A. Mooney, and S. A. Klooster (1993), Terrestrial ecosystem production: A process model based on global satellite and surface data, *Global Biogeochem. Cycles*, 7(4), 811-841, doi:10.1029/93GB02725.
- van der Werf, G. R., Randerson, J. T., Collatz, G. J. and Giglio, L. (2003), Carbon emissions from fires in tropical and subtropical ecosystems. *Global Change Biology*, 9: 547-562. doi:10.1046/j.1365-2486.2003.00604.x
- Jim Randerson research group
- Global Fire Emissions Database (GFED) web page
- Olsen, S. C., and J. T. Randerson (2004), Differences between surface and column atmospheric CO₂ and implications for carbon cycle research, *J. Geophys. Res.*, 109, D02301, doi:10.1029/2003JD003968.
- Giglio, L., van der Werf, G. R., Randerson, J. T., Collatz, G. J., and Kasibhatla, P.: Global estimation of burned area using MODIS active fire observations, *Atmos. Chem. Phys.*, 6, 957-974, doi:10.5194/acp-6-957-2006, 2006.
- van der Werf, G. R., Randerson, J. T., Giglio, L., Collatz, G. J., Kasibhatla, P. S., and Arellano Jr., A. F.: Interannual variability in global biomass burning emissions from 1997 to 2004, *Atmos. Chem. Phys.*, 6, 3423-3441, doi:10.5194/acp-6-3423-2006, 2006.
- L.A Rasmussen, Piecewise integral splines of low degree, *Computers & Geosciences*, Volume 17, Issue 9, 1991, Pages 1255-1263, ISSN 0098-3004, [http://dx.doi.org/10.1016/0098-3004\(91\)90027-B](http://dx.doi.org/10.1016/0098-3004(91)90027-B).
- NASA GFED.CMS CASA project

3 Fire module

Vegetation fires are an important part of the carbon cycle and have been so for many millennia. Even before human civilization began to use fires to clear land for agricultural purposes, most ecosystems were subject to natural wildfires that would rejuvenate old forests and bring important minerals to the soils. When fires

consume part of the landscape in either controlled or natural burning, carbon dioxide (amongst many other gases and aerosols) is released in large quantities. Each year, vegetation fires emit around 2 PgC as CO₂ into the atmosphere, mostly in the tropics. Currently, a large fraction of wildfire is started by humans. This is mostly intentional to clear land for agriculture, or to re-fertilize soils before a new growing season. This important component of the carbon cycle is monitored mostly from space, while sophisticated ‘biomass burning’ models are used to estimate the amount of CO₂ emitted by each fire. Such estimates are then used in CarbonTracker to prescribe the emissions. These emissions are not modified in the optimization (inverse modeling) process.

In CT2015 we introduce the use of multiple fire emissions datasets, and we use higher temporal resolution for fire emissions. The GFED4.1s emissions are modeled at 3-hourly intervals, and FINN emissions are available at daily resolution. In previous CarbonTracker releases, fires were only available as monthly averages.

3.1 Global Fire Emissions Database (GFED)

CT2015 uses GFED4.1s as one of the fire modules to estimate biomass burning. GFED4.1s uses a variant of the CASA biogeochemical model as described in the terrestrial biosphere model documentation to estimate the carbon fuel in various biomass pools. The dataset consists of 1° × 1° gridded monthly burned area, fuel loads, combustion completeness, and fire emissions (Carbon, CO₂, CO, CH₄, NMHC, H₂, NO_x, N₂O, PM2.5, Total Particulate Matter, Total Carbon, Organic Carbon, Black Carbon) for the time period spanning January 1997 - December 2014, of which we currently only use CO₂.

The GFED burned area is based on MODIS satellite observations of fire counts. These, together with detailed vegetation cover information and a set of vegetation specific scaling factors, allow predictions of burned area over the time span that active fire counts from MODIS are available. The relationship between fire counts and burned area is derived, for the specific vegetation types, from a ‘calibration’ subset of 500m resolution burned area from MODIS in the period 2001-2004.

Once burned area has been estimated globally, emissions of trace gases are calculated using the CASA biosphere model. The seasonally changing vegetation and soil biomass stocks in the CASA model are combusted based on the burned area estimate, and converted to atmospheric trace gases using estimates of fuel loads, combustion completeness, and burning efficiency.

For CT2015, we also apply temporal scaling factors updated from Mu *et al.* (2011) to downscale the

GFED4.1s CO₂ emissions from monthly averages to emissions with 3-hourly resolution.

3.2 Fire Inventory from NCAR (FINN)

We use version 1.5 of the Fire Inventory from NCAR (FINN), which supplies global 1-kilometer resolution fire emissions of CO₂ and many other chemical species at daily resolution. Like GFED, FINN uses fires detected by MODIS instruments aboard NASA's polar-orbiting Aqua and Terra satellites. These fire instances are combined with information on land cover type (also from MODIS) which gives fuel loadings and emission factors to convert biomass burned into CO₂ emissions. The area burned for each fire is generally assumed to be 1 km², with exceptions described in Wiedinmyer *et al.* (2011). Finally, a fraction burned is assigned as a function of tree cover.

FINN emissions are available from 2002-2015, but the emissions in 2002 are conspicuously lower than those in following years. FINN developers believe that this may be due to staggered availability of MODIS data. While Terra was in orbit during all of 2002, Aqua was only launched in May of 2002. Data from Aqua thus started to become available only later in 2002. This may have contributed to reduced fire detection before both MODIS streams were available. Consequently, we have chosen to use climatological FINN fires (the 2003-2014 average) during 2000, 2001, and 2002.

3.3 References

- Giglio, L., J. T. Randerson, and G. R. van der Werf, (2013), Analysis of daily, monthly, and annual burned area using the fourth-generation global fire emissions database (GFED4) *J. Geophys. Res. Biogeosci.*, 118, 317328, doi:10.1002/jgrg.20042.
- van der Werf, G. R., Randerson, J. T., Collatz, G. J. and Giglio, L. (2003), Carbon emissions from fires in tropical and subtropical ecosystems. *Global Change Biology*, 9: 547562. doi:10.1046/j.1365-2486.2003.00604.x
- van der Werf, G. R., Randerson, J. T., Giglio, L., Collatz, G. J., Mu, M., Kasibhatla, P. S., Morton, D. C., DeFries, R. S., Jin, Y., and van Leeuwen, T. T.: Global fire emissions and the contribution of deforestation, savanna, forest, agricultural, and peat fires (1997-2009), *Atmos. Chem. Phys.*, 10, 11707-11735, doi:10.5194/acp-10-11707-2010, 2010.
- Akagi, S. K., Yokelson, R. J., Wiedinmyer, C., Alvarado, M. J., Reid, J. S., Karl, T., Crouse, J. D.,

and Wennberg, P. O.: Emission factors for open and domestic biomass burning for use in atmospheric models, *Atmos. Chem. Phys.*, 11, 4039-4072, doi:10.5194/acp-11-4039-2011, 2011.

- Mu, M., Randerson, J. T., van der Werf, G. R., Giglio, L., Kasibhatla, P., Morton, D., Collatz G. J., DeFries, R. S., Hyer, E. J., Prins, E. M., Griffith, D. W. T., Wunch, D., Toon, G. C., Sherlock, V., and Wennberg, P. O. (2011), Daily and 3-hourly variability in global fire emissions and consequences for atmospheric model predictions of carbon monoxide, *J. Geophys. Res.*, 116, D24303, doi:10.1029/2011JD016245.
- Andreae, M. O., and P. Merlet (2001), Emission of trace gases and aerosols from biomass burning, *Global Biogeochem. Cycles*, 15(4), 955-966, doi:10.1029/2000GB001382.
- Giglio, L., van der Werf, G. R., Randerson, J. T., Collatz, G. J., and Kasibhatla, P.: Global estimation of burned area using MODIS active fire observations, *Atmos. Chem. Phys.*, 6, 957-974, doi:10.5194/acp-6-957-2006, 2006.
- van der Werf, G. R., Randerson, J. T., Giglio, L., Collatz, G. J., Kasibhatla, P. S., and Arellano Jr., A. F.: Interannual variability in global biomass burning emissions from 1997 to 2004, *Atmos. Chem. Phys.*, 6, 3423-3441, doi:10.5194/acp-6-3423-2006, 2006.
- Jim Randerson research group
- Global Fire Emissions Database (GFED) web page
- Christine Wiedinmyer, Brad Quayle, Chris Geron, Angie Belote, Don McKenzie, Xiaoyang Zhang, Susan O'Neill, Kristina Klos Wynne, Estimating emissions from fires in North America for air quality modeling, *Atmospheric Environment*, Volume 40, Issue 19, June 2006, Pages 3419-3432, ISSN 1352-2310, <http://dx.doi.org/10.1016/j.atmosenv.2006.02.010>.
- Wiedinmyer, C., S. K. Akagi, R. J. Yokelson, L. K. Emmons, J. A. Al-Saadi, J. J. Orlando, and A. J. Soja. "The Fire Inventory from NCAR (FINN): A High Resolution Global Model to Estimate the Emissions from Open Burning." *Geoscientific Model Development* 4, no. 3 (2011): 625-41.
- FINN web page at NCAR

4 Fossil fuel module

Human beings first influenced the carbon cycle through land-use change. Early humans used fire to control animals and later cleared forests for agriculture. Over the last two centuries, following the industrial

and technical revolutions and continuing global population increase, fossil fuel combustion has become the largest anthropogenic source of CO₂. In 2013, fossil fuel combustion was responsible for nearly 10 billion tons of carbon emitted to the atmosphere. Coal, oil and natural gas combustion are the most common energy sources in both developed and developing countries. Various sectors of the economy rely on fossil fuel combustion: power generation, transportation, residential & commercial building heating, and industrial processes. According to the Carbon Dioxide Information and Analysis Center (CDIAC), world emissions of CO₂ from fossil fuel burning, cement manufacturing, and flaring reached 9.4 PgC yr⁻¹ (one PgC=10¹⁵ grams of carbon) in 2011 (Boden *et al.*, 2015). Estimates extrapolated by the CarbonTracker team indicate that [the global total emissions for 2012, 2013, and 2014 are 9.6 PgC yr⁻¹, 9.7 PgC yr⁻¹, and 9.8 PgC yr⁻¹ respectively](#). The 2014 emissions are 59% larger than those in 1990. U.S. input of CO₂ to the atmosphere from fossil fuel burning in 2014 was 1.4 PgC, representing 14% of the global total. North American emissions have remained nearly constant since 2000, with a slight decrease in recent years. On the other hand, emissions from developing economies such as the People's Republic of China have been increasing. Emissions from China in 2014 were 2.6 PgC yr⁻¹, representing 27% of the global total.

Despite the recent economic slowdown, which affected many countries starting in 2008, fossil fuel emissions have rebounded, and in many parts of the world continue to increase. The [Department of Energy's International Energy Outlook 2013](#) projects that the global total source will reach 12.4 PgC yr⁻¹ in 2040. This may be an underestimate, however, as that same report projects 2020 emissions of 9.9 PgC yr⁻¹, a figure that was nearly reached already in 2014.

In many global and regional carbon flux estimation systems, including CarbonTracker, fossil fuel CO₂ emissions are not optimized. Instead, these emissions are imposed and are not subject to revision by the estimation framework. Thus it is vital that fossil fuel CO₂ emissions are prescribed accurately, so that flux estimates for the land biosphere and oceans are robust. The fossil fuel emissions source data we use are available on an annually-integrated global and national basis. This aggregate information needs to be gridded before being incorporated into CarbonTracker. The major uncertainty in this process is distributing the national-annual emissions spatially across a nation and temporally into monthly contributions. In CT2015, two different fossil fuel CO₂ emissions datasets were used to help assess the uncertainty in this mapping process. These two emissions products are called the "Miller" and "ODIAC" emissions datasets. These two datasets have nearly identical global and national emissions for each year, but differ in how those emissions are distributed spatially and temporally.

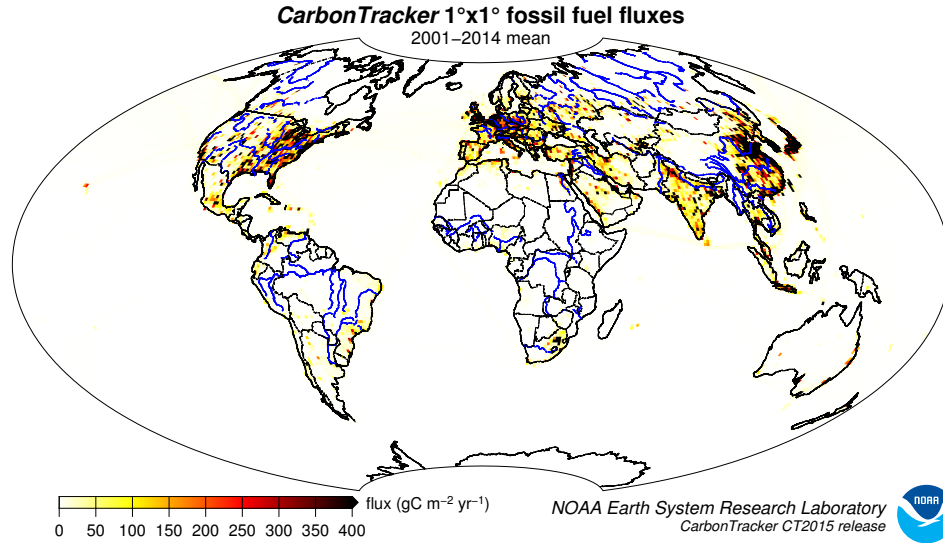


Figure 4: Spatial distribution of fossil fuel emissions. This is a spatial average of the Miller and ODIAC emissions inventories.

Whereas previous CarbonTracker releases used monthly-constant fossil fuel emissions, in CT2015 we introduce the use of temporal scaling factors to simulate day-of-week and diurnal variability for those emissions. These “Temporal Improvements for Modeling Emissions by Scaling” (TIMES) scaling factors, introduced by Nassar *et al.* (2013), are applied to both the Miller and ODIAC emissions modules. The scaling factors consist of seven day-of-week global scaling factor maps, and 24 hourly global scaling factor maps to represent the diurnal cycle. For use in TM5, the hourly scaling factors were aggregated to three-hourly factors to accommodate the natural time step of the model.

4.1 The “Miller” emissions dataset

- **Global Totals** The Miller fossil fuel emission inventory is derived from independent global total and spatially-resolved inventories. Annual global total fossil fuel CO₂ emissions are from the Carbon Dioxide Information and Analysis Center (CDIAC, Boden *et al.* 2013) which extend through 2010. In order to extrapolate these fluxes through 2014, we extrapolate using the percentage increase or decrease for each fuel type (solid, liquid, and gas) in each country from the 2015 BP Statistical Review of World Energy for 2011-2014. To estimate emissions for the first two months of 2015 (required by CarbonTracker’s 5-week assimilation window), no increase is applied to 2014 values.
- **Spatial Distribution** Miller fossil-fuel CO₂ fluxes are spatially distributed in two steps: First, the coarse-scale country totals through 2010 (from Boden *et al.* 2013) are mapped onto a 1° × 1° grid

according to the spatial patterns from the EDGAR v4.2 inventories (European Commission, 2009). EDGAR provides annual emissions estimates at $1^\circ \times 1^\circ$ resolution, but their totals do not agree with those from CDIAC. The CDIAC country-by-country totals sum to about 95% of the global total emissions; the remaining 5% is mapped to global shipping routes according to EDGAR.

- **Temporal Distribution** For North America between 30 and 60°N , the Miller system imposes a seasonal cycle derived from the first and second harmonics (Thoning *et al.*, 1989) of the Blasing *et al.* (2005) analysis for the United States. The Blasing analysis has $\sim 10\%$ higher emissions in winter than in summer. This scheme defines a fixed fraction of emissions for each month, so while the shape of the annual cycle is invariant, the amplitude of that cycle scales with the annual total emissions. For Eurasia, a set of seasonal emissions factors from EDGAR distributed by emissions sector is used to define fossil fuel seasonality. As in North America, this seasonality is imposed only from 30 - 60°N . The Eurasian seasonal amplitude is about 25% , significantly larger than that in North America, owing to the absence of a secondary summertime maximum due to air conditioning. See Figure 5 for the resulting time series of fossil fuel emissions. In order to avoid discontinuities in the fossil fuel emissions between consecutive years, a spline curve that conserves annual totals (Rasmussen 1991) is fit to seasonal emissions in each $1^\circ \times 1^\circ$ grid cell.

4.2 The “ODIAC” emissions dataset

- **Global Totals** The ODIAC fossil fuel emission inventory (Oda and Maksyutov, 2011) is also derived from independent global and country emission estimates from CDIAC, but national emission estimates used were taken from the year 2010 edition of CDIAC estimates. Annual country total fossil fuel CO_2 emissions from CDIAC which extend through 2007, were extrapolated through 2014 using the BP Statistical Review of World Energy. The difference between the CDIAC global total and country-by-country totals were ascribed to the entire emissions fields. The same adjustment was done for the year extrapolated using using the CDIAC global total (2007-2011).
- **Spatial Distribution** ODIAC emissions are spatially distributed using many available “proxy data” that explain spatial extent of emissions according to emission types (emissions over land, gas flaring, aviation and marine bunker). Emissions over land were distributed in two steps: First, emissions attributable to power plants were mapped using geographical locations (latitude and longitude) provided

by the global power plant dataset [CARbon Monitoring and Action, CARMA](#). Next, the remaining land emissions (*i.e.* land total minus power plant emissions) were distributed using nightlight imagery collected by U.S. Air Force Defense Meteorological Satellite Project (DMSP) satellites. Emissions from gas flaring were also mapped using nightlight imagery. Emissions from aviation were mapped using flight tracks adopted from UK AERO2k air emission inventory. It should be noted that currently, air traffic emissions are emitted at ground level within CarbonTracker. Emissions from marine bunker fuels are placed entirely in the ocean basins along shipping routes according to patterns from the EDGAR database.

- **Temporal Distribution** The CDIAC estimates used for mapping emissions in ODIAC only describe how much CO₂ was emitted in a given year. To present seasonal changes in emissions, we used the CDIAC 1° × 1° monthly fossil fuel emission inventory (Andres *et al.* 2011). The CDIAC monthly data utilizes the top 20 emitting countries' fuel (coal, oil and gas) consumption statistics available to estimate seasonal change in emissions. Monthly emission numbers at each pixel were divided by annual total and then a fraction to annual total was obtained. Monthly emissions in the ODIAC inventory were derived by multiplying this fraction by the emission in each grid cell.

4.3 Uncertainties

Marland (2008) attached an uncertainty of about 5% (95% confidence interval; approximately 2- σ) to the global total fossil fuel source. Recent estimates by Andres *et al.* (2014) put a larger uncertainty of 8.4% (2- σ) on the CDIAC global total. Uncertainties for individual regions of the world, and for sub-annual time periods are likely to be larger. Additional uncertainties are introduced when the emissions are distributed in space and time. In the Miller dataset, the overall Eurasian seasonality is highly uncertain, but most likely a better representation than assuming no emission seasonality at all. Similarly, the use of the CDIAC monthly emission dataset for modeling seasonality introduces additional uncertainty in ODIAC. The additional uncertainty for the global total in the monthly CDIAC emission, which is solely due to the method for estimating seasonality, is reported as 6.4% (Andres *et al.* 2011). As mentioned earlier, fossil fuel emissions are not optimized in the current CarbonTracker system, similar to nearly all carbon data analysis systems. Spatial and temporal atmospheric CO₂ gradients arise from terrestrial biosphere and fossil-fuel sources. These gradients, which are interpreted by CarbonTracker, are difficult to attribute to one or the other cause.

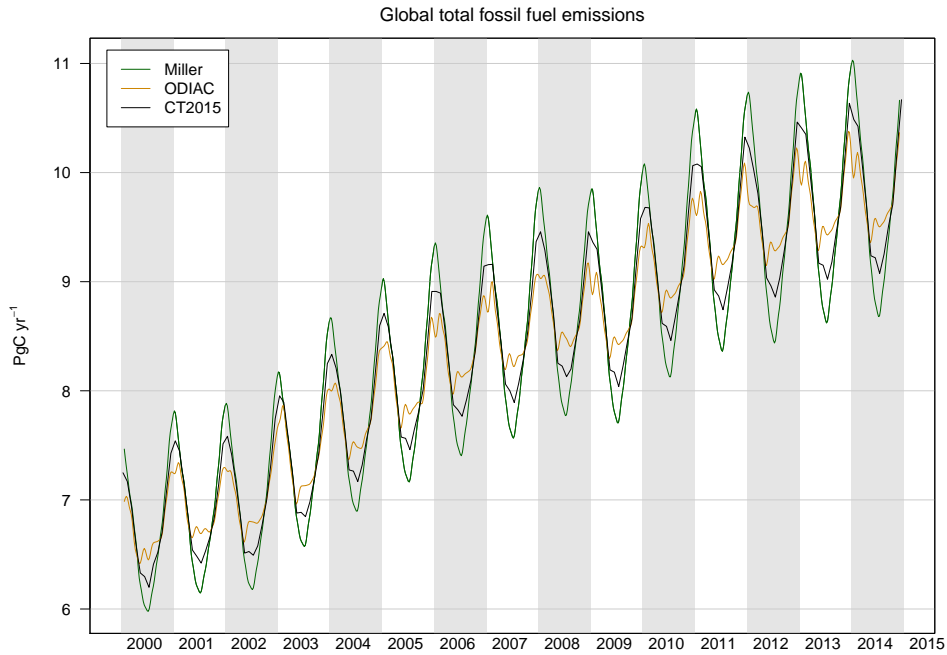


Figure 5: Time series of global fossil fuel emissions. The Miller (green) and ODIAC (tan) estimates are each used by half of the sixteen inversions in the CT2015 suite, so the CT2015 (black) inventory is effectively an average of Miller and ODIAC. Note that fossil fuel emissions are not optimized in CarbonTracker.

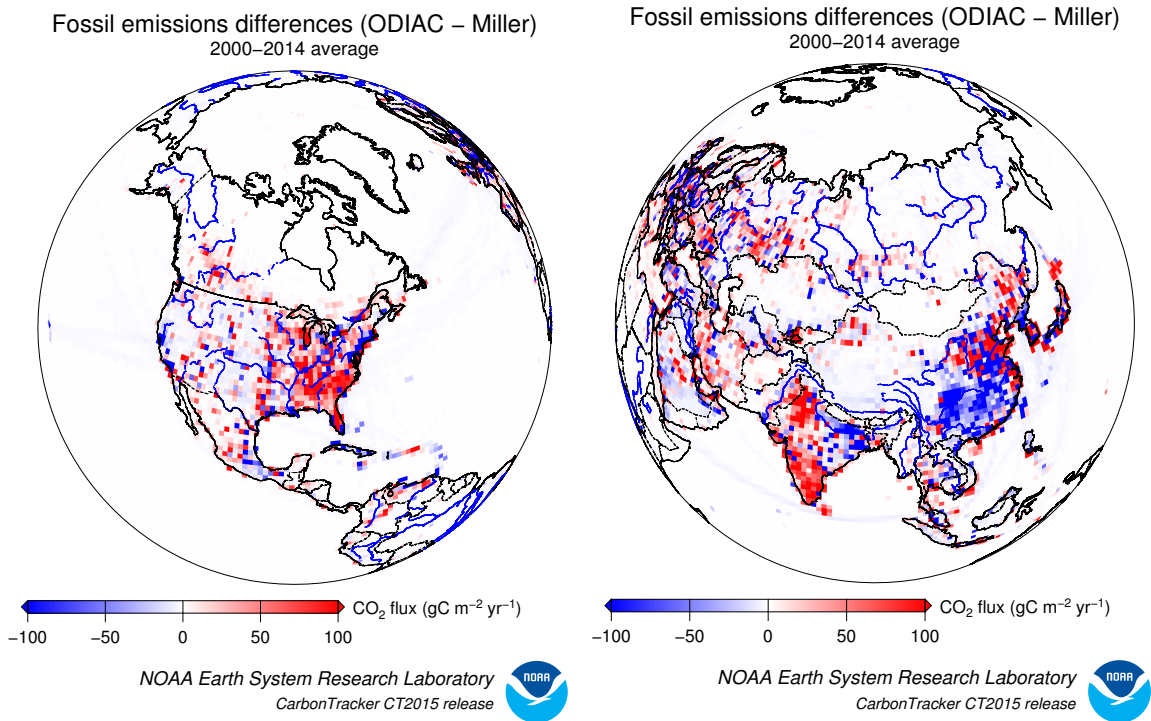


Figure 6: Spatial differences in long-term mean fossil fuel emissions between the two priors. Note that both the Miller and ODIAC emissions inventories use the same country totals, but have different models for spatial distribution of that flux within countries.

This is because the biospheric and anthropogenic sources are often co-located, especially in the temperate Northern Hemisphere. Given that surface CO₂ flux due to biospheric activity and oceanic exchange is much more uncertain compared to fossil fuel emissions, CarbonTracker, like most current carbon dioxide data assimilation systems, does not optimize fossil fuel emissions. The contribution of CO₂ from fossil fuel burning to observed CO₂ mole fractions is considered known. However, for the first time in CarbonTracker, an effort is made to account for some aspects of fossil fuel uncertainty by using two different fossil fuel estimates as detailed above. From a technical point of view, extra land biosphere prior flux uncertainty is included in the system to represent the random errors in fossil fuel emissions. Eventually, fossil fuel emissions could be optimized within CarbonTracker, especially with the addition of ¹⁴CO₂ observations as constraints.

4.4 References

- Nassar, R., L. Napier-Linton, K. R. Gurney, R. J. Andres, T. Oda, F. R. Vogel, and F. Deng (2013), Improving the temporal and spatial distribution of CO₂ emissions from global fossil fuel emission data sets, *J. Geophys. Res. Atmos.*, 118, 917933, doi:10.1029/2012JD018196.
- CDIAC Annual Global and National fluxes
- DOE Energy Information Administration (EIA)
- BP Statistical Review of World Energy
- EDGAR Database
- CDIAC (Blasing *et al.*) Monthly USA fluxes
- L.A Rasmussen, Piecewise integral splines of low degree, *Computers & Geosciences*, Volume 17, Issue 9, 1991, Pages 1255-1263, ISSN 0098-3004, [http://dx.doi.org/10.1016/0098-3004\(91\)90027-B](http://dx.doi.org/10.1016/0098-3004(91)90027-B).
- Thoning, K. W., P. P. Tans, and W. D. Komhyr (1989), Atmospheric carbon dioxide at Mauna Loa Observatory: 2. Analysis of the NOAA GMCC data, 1974-1985, *J. Geophys. Res.*, 94(D6), 8549-8565, doi:10.1029/JD094iD06p08549.
- Marland, G. (2008), Uncertainties in Accounting for CO₂ from Fossil Fuels, *Journal of Industrial Ecology*, 12(2), 136-139.
- Boden, T.A., G. Marland, and R.J. Andres. 2015. Global, Regional, and National Fossil-Fuel CO₂ Emissions. Carbon Dioxide Information Analysis Center, Oak Ridge National Laboratory, U.S. Department of Energy, Oak Ridge, Tenn., U.S.A. DOI: 10.3334/CDIAC/00001_V2015

- [CDIAC Preliminary 2011 and 2012 Global and National Estimates](#))
- [The Center for Global Development, CARbon Monitoring Action \(CARMA\) power plant database](#)
- [DMSP satellite nightlight data](#)
- [Centre for Air Transport and the Environment \(CATE\), AERO2k aviation emissions inventory](#)
- [Andres, R. J., J. S. Gregg, L. Losey, G. Marland, T. A. Boden \(2011\) Monthly, global emissions of carbon dioxide from fossil fuel consumption. *Tellus B*, 63:309-327. doi: 10.1111/j.1600-0889.2011.00530.x.](#)
- [Andres R.J., T.A. Boden, G. Marland, Monthly Fossil-Fuel CO₂ Emissions: Mass of Emissions Gridded by One Degree Latitude by One Degree Longitude, doi:10.3334/CDIAC/ffe.MonthlyMass.2015](#)
- [Oda, T. and Maksyutov, S.: A very high-resolution \(1 km × 1 km\) global fossil fuel CO₂ emission inventory derived using a point source database and satellite observations of nighttime lights, *Atmos. Chem. Phys.*, 11, 543-556, doi:10.5194/acp-11-543-2011, 2011.](#)
- [European Commission, Joint Research Centre \(JRC\)/Netherlands Environmental Assessment Agency \(PBL\). \(2009\) Emission Database for Global Atmospheric Research \(EDGAR\), release version 4.0](#)
- [Andres, Robert J.; Boden, Thomas A.; Higdson, David \(2014\). A new evaluation of the uncertainty associated with CDIAC estimates of fossil fuel carbon dioxide emission. *Tellus B*, 66, doi:10.3402/tellusb.v66.23616](#)

5 Oceans module

The oceans play an important role in the Earth's carbon cycle. They are the largest long-term sink for carbon and have an enormous capacity to store and redistribute CO₂ within the Earth system. Oceanographers estimate that about 48% of the CO₂ from fossil fuel burning has been absorbed by the ocean (Sabine *et al.*, 2004). The dissolution of CO₂ in seawater shifts the balance of the ocean carbonate equilibrium towards a more acidic state with a lower pH. This effect is already measurable (Caldeira and Wickett, 2003), and is expected to become an acute challenge to shell-forming organisms over the coming decades and centuries. Although the oceans as a whole have been a relatively steady net carbon sink, CO₂ can also be released from oceans depending on local temperatures, biological activity, wind speeds, and ocean circulation. These processes are all considered in CarbonTracker, since they can have significant effects on the ocean sink. Improved estimates of the air-sea exchange of carbon in turn help us to understand variability of both the atmospheric burden of CO₂ and terrestrial carbon exchange.

The initial release of CarbonTracker (CT2007) used climatological estimates of CO₂ partial pressure in

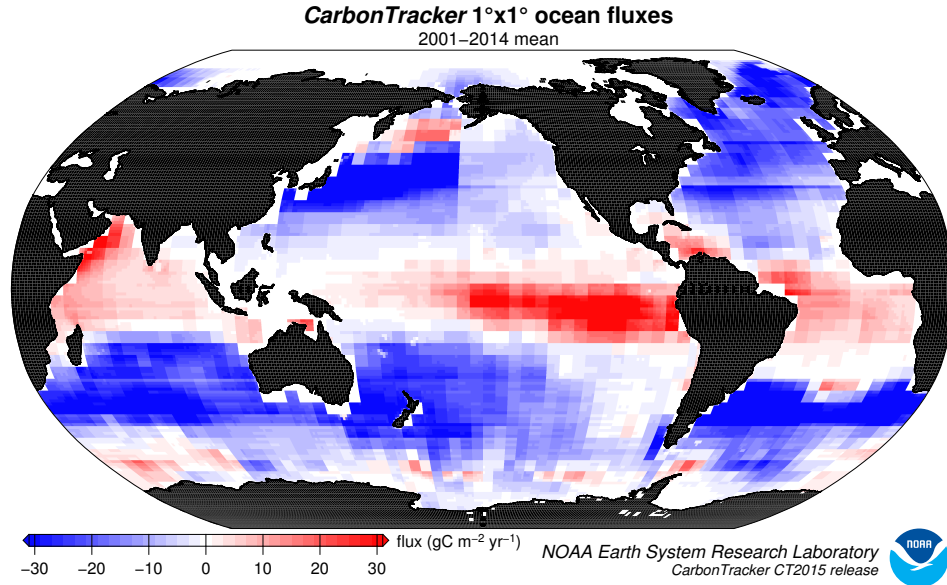


Figure 7: Posterior long-term mean ocean fluxes from CarbonTracker. The pattern of air-sea exchange of CO_2 averaged over the time period indicated, as estimated by CarbonTracker. Negative fluxes (blue colors) represent CO_2 uptake by the ocean, whereas positive fluxes (red colors) indicate regions in which the ocean is a net source of CO_2 to the atmosphere. Units are $\text{gC m}^{-2} \text{yr}^{-1}$.

surface waters ($p\text{CO}_2$) from Takahashi *et al.* (2002) to compute a first-guess air-sea flux. This air-sea $p\text{CO}_2$ disequilibrium was modulated by a surface barometric pressure correction before being multiplied by a gas-transfer coefficient to yield a flux. Starting with CT2007B and continuing through the CT2011_o release, the air-sea $p\text{CO}_2$ disequilibrium was imposed from analysis of ocean inversions (“OIF”, *cf.* Jacobson *et al.*, 2007) results, with short-term flux variability derived from the atmospheric model wind speeds via the gas transfer coefficient. The barometric pressure correction was removed so that climatological high- and low-pressure cells did not bias the long-term means of the first guess fluxes.

In CT2015, two models are used to provide prior estimates of air-sea CO_2 flux. The OIF scheme provides one of these flux priors, and the other is an updated version of the Takahashi *et al.* $p\text{CO}_2$ climatology.

5.1 Air-sea gas exchange

Oceanic uptake of CO_2 in CarbonTracker is computed using air-sea differences in partial pressure of CO_2 inferred either from ocean inversions (called “OIF” henceforth), or from a compilation of direct measurements of seawater $p\text{CO}_2$ (called “ $p\text{CO}_2$ -clim” henceforth). These air-sea partial pressure differences are combined with a gas transfer velocity computed from wind speeds in the atmospheric transport model to compute fluxes of carbon dioxide across the sea surface.

In either method, the first-guess fluxes have no interannual variability (IAV) other than a smooth trend. IAV in oceanic CO₂ flux is due to anomalies in surface $p\text{CO}_2$, such as those that occur in the tropical eastern Pacific during an El Niño, and to associated variability in winds, ocean circulation, and sea-surface properties. In CarbonTracker, only the surface winds (and hence gas transfer), manifest these interannual anomalies; the remaining IAV of flux must be inferred from atmospheric CO₂ signals.

In the following sections we describe the two ocean flux prior models. We then describe the air-sea gas transfer velocity parameterization and discuss details of the inversion methodology specific to oceanic exchange of CO₂.

5.2 OIF: the Ocean Inversion Fluxes prior

For the OIF prior, long-term mean air-sea fluxes and the uncertainties associated with them are derived from the ocean interior inversions reported in Jacobson *et al.* (2007). These ocean inversion flux estimates are composed of separate preindustrial (natural) and anthropogenic flux inversions based on the methods described in Gloor *et al.* (2003) and biogeochemical interpretations of Gruber, Sarmiento, and Stocker (1996). The uptake of anthropogenic CO₂ by the ocean is assumed to increase in proportion to atmospheric CO₂ levels, consistent with estimates from ocean carbon models.

OIF contemporary $p\text{CO}_2$ fields were computed by summing the preindustrial and anthropogenic flux components from inversions using five different configurations of the Princeton/GFDL MOM3 ocean general circulation model (Pacanowski and Gnanadesikan, 1998), then dividing by a gas transfer velocity computed from the European Centre for Medium-Range Weather Forecasts (ECMWF) ERA40 reanalysis. There are two small differences in first-guess fluxes in this computation from those reported in Jacobson *et al.* (2007). First, the five OIF estimates all used Takahashi *et al.* (2002) $p\text{CO}_2$ estimates to provide high-resolution patterning of flux within inversion regions (the alternative “forward” model patterns were not used). To good approximation, this choice only affects the spatial and temporal distribution of flux within each of the 30 ocean inversion regions, not the magnitude of the estimated flux. Second, wind speed differences between the ERA40 product used in the offline analysis and the ECMWF operational model used in the online CarbonTracker analysis result in small deviations from the OIF estimates.

Other than the smooth trend in anthropogenic flux assumed by the OIF results, interannual variability (IAV) in the first guess ocean flux comes entirely from wind speed effects on the gas transfer velocity. This is because the ocean inversions retrieve only a long-term mean and smooth trend.

5.3 $p\text{CO}_2$ -Clim: Takahashi *et al.* (2009) climatology prior

The $p\text{CO}_2$ -Clim prior is derived from the Takahashi *et al.* (2009) climatology of seawater $p\text{CO}_2$. This climatology was created from about 3 million direct observations of seawater $p\text{CO}_2$ around the world between 1970 and 2007. With the exception of measurements in the Bering Sea, these observations were all linearly extrapolated to the corresponding month of the year 2000 by assuming a constant trend of $1.5 \mu\text{atm yr}^{-1}$. This set of global monthly measurements corrected to the reference year 2000 was then interpolated onto a regular grid using a modeled surface current field.

The Takahashi *et al.* (2009) product goes beyond providing this estimate of surface water $p\text{CO}_2$. They also compute climatological air-sea exchange of CO_2 by using the GLOBALVIEW- CO_2 atmospheric carbon dioxide product to compute air-sea $\Delta p\text{CO}_2$, sea surface properties inferred from ocean climatologies, and winds from atmospheric reanalysis to estimate gas-transfer velocity. Unlike many other atmospheric analyses, we have chosen not to use the climatological fluxes as our prior, nor to use the climatological $\Delta p\text{CO}_2$. Instead, we take only the seawater $p\text{CO}_2$ distribution from the Takahashi *et al.* climatology—our atmospheric model provides both $p\text{CO}_2$ in the air at the sea surface and the winds needed to estimate gas transfer. Seawater $p\text{CO}_2$ is extrapolated from 2000 to the actual year of the CarbonTracker simulation using a presumed increase of $1.5 \mu\text{atm yr}^{-1}$ at every point in the global ocean. This is the same trend used in Takahashi *et al.* to normalize observations from many years to the reference year of the analysis (2000).

5.4 Gas-transfer velocity and ocean surface properties

Both priors use CO_2 solubilities and Schmidt numbers computed from World Ocean Atlas 2009 (WOA09) climatological fields of sea surface temperature (Locarnini *et al.*, 2010) and sea surface salinity (Antonov *et al.*, 2010) fields. Gas transfer velocity in CarbonTracker is parameterized as a quadratic function of wind speed following Wanninkhof (1992), using the formulation for instantaneous winds. Gas exchange is computed every 3 hours using wind speeds from the ECMWF operational model as represented by the atmospheric transport model.

Air-sea transfer is inhibited by the presence of sea ice, and for this work fluxes are scaled by the daily sea ice fraction in each gridbox provided by the ECMWF forecast data.

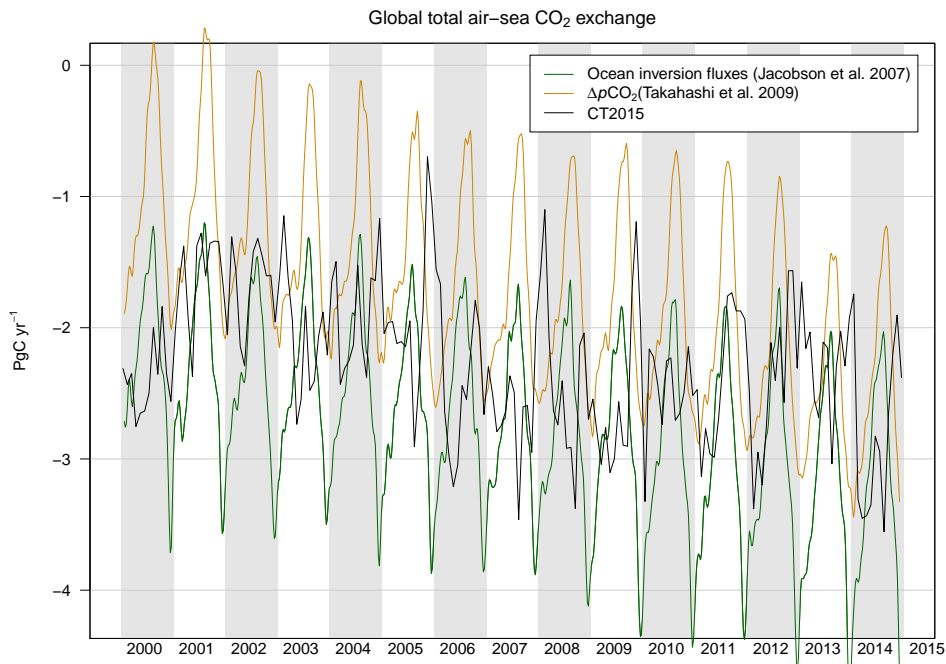


Figure 8: Comparison of air-sea flux priors and the CT2015 posterior. Global CO₂ uptake by the ocean, expressed in PgC yr⁻¹. Positive flux represents a gain of CO₂ to the atmosphere, and the negative numbers here indicate that the ocean is a sink of CO₂. While both priors manifest similar trends of increasing oceanic uptake of CO₂, the OIF prior (in green) has more oceanic uptake and a greater annual cycle than the *p*CO₂-clim prior (in tan). The CT2015 across-model posterior estimate is shown in black for comparison.

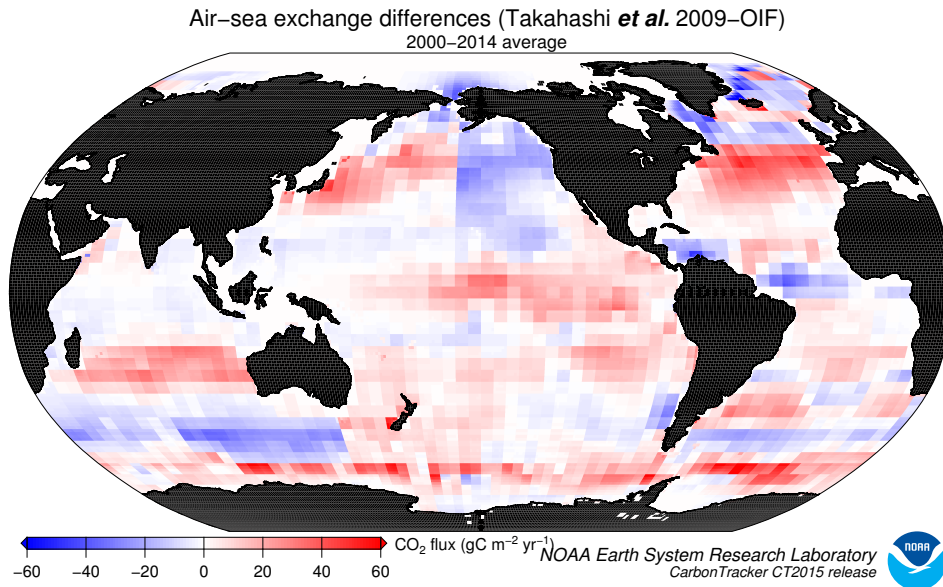


Figure 9: Differences in long-term mean ocean fluxes between the two priors. Red indicates areas where the *p*CO₂-clim prior has less oceanic uptake (or more outgassing to the atmosphere) than the OIF prior, and blue represents the opposite. Units are gC m⁻² yr⁻¹.

5.5 Specifics of the inversion methodology related to air-sea CO₂ fluxes

The first-guess fluxes described here are subject to scaling during the CarbonTracker optimization process, in which atmospheric CO₂ mole fraction observations are combined with transport simulated by the atmospheric model to infer flux signals. Prior air-sea fluxes are adjusted within each of the 30 ocean inversion regions. In this process, signals of terrestrial flux in atmospheric CO₂ distribution can be erroneously interpreted as being caused by oceanic fluxes. This flux “aliasing” or “leakage” is evident in some regions as a change in the shape of the seasonal cycle of air-sea flux.

Prior uncertainties for the OIF and *p*CO₂-clim models are specified as uncertainties on scaling factors multiplying net CO₂ flux in each of the 30 ocean inversion regions. The *p*CO₂-clim prior has independent regional uncertainties (a diagonal prior covariance matrix), with the uncertainty standard deviation on each region set to 40%. The OIF prior uncertainty has a fully-covariate covariance matrix with off-diagonal elements representing the results of the ocean inversion of Jacobson *et al.* (2007). The pre-industrial flux uncertainty is time-independent, but the anthropogenic flux uncertainty grows in time as anthropogenic flux uptake increases. The latter is scaled to the simulation date, then added to the former. Total uncertainties are consistent with the Jacobson *et al.* (2007) results.

5.6 References

- [NOAA Pacific Marine Environmental Laboratory](#)
- [Ocean Acidification](#)
- Locarnini, R. A., A. V. Mishonov, J. I. Antonov, T. P. Boyer, H. E. Garcia, O. K. Baranova, M. M. Zweng, and D. R. Johnson, 2010. World Ocean Atlas 2009, Volume 1: Temperature. S. Levitus, Ed. NOAA Atlas NESDIS 68, U.S. Government Printing Office, Washington, D.C., 184 pp.
- Antonov, J. I., D. Seidov, T. P. Boyer, R. A. Locarnini, A. V. Mishonov, H. E. Garcia, O. K. Baranova, M. M. Zweng, and D. R. Johnson, 2010. World Ocean Atlas 2009, Volume 2: Salinity. S. Levitus, Ed. NOAA Atlas NESDIS 69, U.S. Government Printing Office, Washington, D.C., 184 pp.
- Caldeira, K., and M. E. Wickett (2003), Anthropogenic carbon and ocean pH, *Nature*, 425365-365, doi:10.1038/425365a
- GLOBALVIEW-CO2 Cooperative Atmospheric Data Integration Project - Carbon Dioxide. CD-ROM, NOAA ESRL, Boulder, Colorado (Also available on Internet via anonymous FTP to ftp.cmdl.noaa.gov,

Path: ccg/co2/GLOBALVIEW), 2011.

- Gloor, M., N. Gruber, J. Sarmiento, C. L. Sabine, R. A. Feely, and C. Rdenbeck (2003), A first estimate of present and preindustrial air-sea CO₂ flux patterns based on ocean interior carbon measurements and models, *Geophysical Research Letters*, 30, doi: 10.1029/2002GL015594.
- Gruber, N., J. L. Sarmiento, and T. F. Stocker (1996), An improved method for detecting anthropogenic CO₂ in the oceans, *Global Biogeochem. Cycles*, 10(4), 809837, doi:10.1029/96GB01608.
- Jacobson, A. R., S. E. Mikaloff Fletcher, N. Gruber, J. L. Sarmiento, and M. Gloor (2007), A joint atmosphere-ocean inversion for surface fluxes of carbon dioxide: 1. Methods and global-scale fluxes, *Global Biogeochem. Cycles*, 21, GB1019, doi:10.1029/2005GB002556.
- Ronald C. Pacanowski and Anand Gnanadesikan, 1998: Transient Response in a Z-Level Ocean Model That Resolves Topography with Partial Cells. *Mon. Wea. Rev.*, 126, 32483270. doi: [http://dx.doi.org/10.1175/10493\(1998\)126<3248:TRIAZLj2.0.CO;2](http://dx.doi.org/10.1175/10493(1998)126<3248:TRIAZLj2.0.CO;2)
- Sabine, C. L., R. A. Feely, N. Gruber, R. M. Key, K. Lee, J. L. Bullister, R. Wanninkhof, C. S. Wong, D. W. R. Wallace, B. Tilbrook, F. J. Millero, T. H. Peng, A. Kozyr, T. Ono, and A. F. Rios (2004), The oceanic sink for anthropogenic CO₂, *Science*, 305, 367-371, DOI: 10.1126/science.1097403
- Taro Takahashi, Stewart C. Sutherland, Colm Sweeney, Alain Poisson, Nicolas Metzl, Bronte Tilbrook, Nicolas Bates, Rik Wanninkhof, Richard A. Feely, Christopher Sabine, Jon Olafsson, Yukihiro Nojiri, Global seaair CO₂ flux based on climatological surface ocean *p*CO₂, and seasonal biological and temperature effects, *Deep Sea Research Part II: Topical Studies in Oceanography*, Volume 49, Issues 910, 2002, Pages 1601-1622, ISSN 0967-0645, [http://dx.doi.org/10.1016/S0967-0645\(02\)00003-6](http://dx.doi.org/10.1016/S0967-0645(02)00003-6).
- Taro Takahashi, Stewart C. Sutherland, Rik Wanninkhof, Colm Sweeney, Richard A. Feely, David W. Chipman, Burke Hales, Gernot Friederich, Francisco Chavez, Christopher Sabine, Andrew Watson, Dorothee C.E. Bakker, Ute Schuster, Nicolas Metzl, Hisayuki Yoshikawa-Inoue, Masao Ishii, Takashi Midorikawa, Yukihiro Nojiri, Arne Krtzinger, Tobias Steinhoff, Mario Hoppema, Jon Olafsson, Thorarinn S. Arnarson, Bronte Tilbrook, Truls Johannessen, Are Olsen, Richard Bellerby, C.S. Wong, Bruno Delille, N.R. Bates, Hein J.W. de Baar, Climatological mean and decadal change in surface ocean *p*CO₂, and net sea-air CO₂ flux over the global oceans, *Deep Sea Research Part II: Topical Studies in Oceanography*, Volume 56, Issues 810, April 2009, Pages 554-577, ISSN 0967-0645, <http://dx.doi.org/10.1016/j.dsr2.2008.12.009>.

- [Wanninkhof, R. \(1992\), Relationship between wind speed and gas exchange over the ocean, J. Geophys. Res., 97\(C5\), 73737382, doi:10.1029/92JC00188.](#)

6 Atmospheric transport

The link between observations of CO₂ in the atmosphere and the exchange of CO₂ at the Earth's surface is transport in the atmosphere: storm systems, cloud complexes, and weather of all sorts cause winds that transport CO₂ around the world. As a result, local surface CO₂ exchange events like fires, forest growth, and ocean upwelling can have impacts at remote locations. To simulate the winds and the weather, CarbonTracker uses sophisticated numerical models that are driven by the daily weather forecasts from the specialized meteorological centers of the world. Since CO₂ does not decay or react in the lower atmosphere, the influence of emissions and uptake in locations such as North America and Europe are ultimately seen in our measurements even at the South Pole. Getting the transport of CO₂ just right is an enormous challenge, and costs us almost all of the computer resources for CarbonTracker. To represent the atmospheric transport, we use the Transport Model 5 (TM5). This is a community-supported model whose development is shared among many scientific groups with different areas of expertise. TM5 is used for many applications other than CarbonTracker, including forecasting air-quality, studying the dispersion of aerosols in the tropics, tracking biomass burning plumes, and predicting pollution levels that future generations might have to deal with.

6.1 TM5 offline tracer transport model

TM5 is an offline global chemical transport model with two-way nested grids. In this global model, regions for which high-resolution simulations are desired can be nested in the coarser global grid. The advantage to this approach is that transport simulations can be performed with a regional focus without the need for boundary conditions. Further, this approach allows measurements outside the "zoom" domain to constrain regional fluxes in the data assimilation, and ensures that regional estimates are consistent with global constraints. TM5 is based on a predecessor model TM3, with improvements in the advection scheme, vertical diffusion parameterization, and meteorological preprocessing of the wind fields ([Krol *et al.*, 2005](#)).

The model is developed and maintained jointly by the [Institute for Marine and Atmospheric Research Utrecht \(IMAU, The Netherlands\)](#), the [Joint Research Centre \(JRC, Italy\)](#), the [Royal Netherlands Mete-](#)

orological Institute (KNMI), the Netherlands Institute for Space Research (SRON) NOAA Earth System Research Laboratory (ESRL).

In CarbonTracker, TM5 separately simulates advection, deep and shallow convection, and vertical diffusion in both the planetary boundary layer and free troposphere. The carbon dioxide concentrations predicted by CarbonTracker do not feed back onto these predictions of winds.

Prior to use in TM5, ECMWF meteorological data are preprocessed into coarser grids, with attention to retrieving a flow that conserves tracer mass. Like most numerical weather prediction models, advection in the parent ECMWF model is not strictly mass-conserving, so this step is crucial. In CarbonTracker, TM5 is currently run at a global 3° longitude \times 2° latitude resolution with a nested regional grid over North America at $1^\circ \times 1^\circ$ resolution (Figure 10). TM5 uses a dynamically-variable time step with a maximum length of 90 minutes. This overall timestep is dynamically reduced to maintain numerical stability, generally during times of high wind speeds. The timestep is divided in half and individual advection, diffusion, convection, and chemistry operators are applied symmetrically in each half step. Furthermore, transport operators in nested grids are modeled at shorter timesteps, so processes at the finest scales are conducted at an effective timestep of one-quarter the overall timestep. See Krol *et al.* (2005) for details.

The winds which drive TM5 come from the ERA-interim reanalysis implemented in the European Centre for Medium-Range Weather Forecasts (ECMWF) modeling system. The ERA-Interim reanalysis uses Cy31r2 version of the ECMWF Integrated Forecast System (IFS) model, which was used for the operational forecasts up until June 2007. That model uses a 30-minute time step and a spectral T255 horizontal resolution, which corresponds to approximately 79 km spacing on a reduced Gaussian grid. This version of the IFS has 60 model layers in the vertical, of which TM5 uses a 25-layer subset. These levels are listed in Table 1.

6.2 Convective flux fix

Until recently, TM5 was known to have difficulties representing the global surface distribution of sulfur hexafluoride (SF_6 , see Figure 11 and Peters *et al.*, 2004). SF_6 is a nearly inert tracer in the atmosphere, with very small surface and atmospheric sinks and an atmospheric lifetime of about 1,000 years. Consequently, its global budget is very well known from observations alone. It is thought to be released mainly via leakage from electrical transformers. Since the electrical distribution system is closely tied to fossil fuel consumption, SF_6 is often considered an analog for fossil fuel CO_2 in the atmosphere. It is useful for understanding

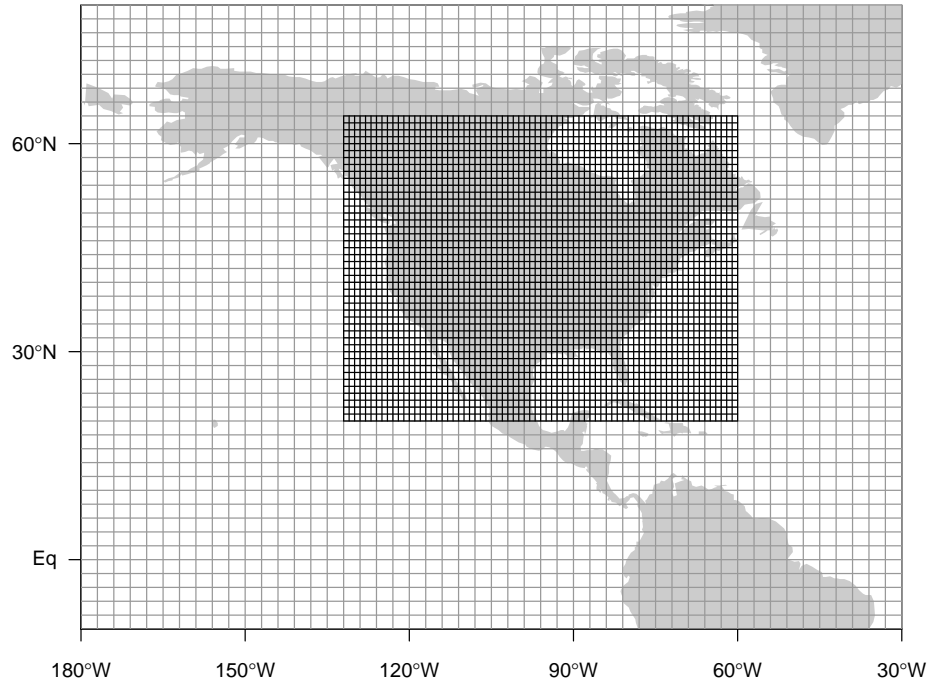


Figure 10: Nested grids used in CarbonTracker over North America. TM5 is a global model, but it employs nested grids to provide higher resolution over regions of interest. This figure shows the $1^\circ \times 1^\circ$ nested regional grid over North America and a portion of the global 3° longitude \times 2° latitude grid.

Model Level	Mean Height (m)	Model Level	Mean Height (m)
1	25	14	9114
2	103	15	10588
3	247	16	12184
4	480	17	13928
5	814	18	15843
6	1259	19	17983
7	1822	20	20412
8	2508	21	24433
9	3317	22	30003
10	4248	23	35895
11	5300	24	43210
12	6467	25	123622
13	7741		

Table 1: Mean mid-level heights above ground in meters for the TM5 model using ERA-interim transport.

the rate at which Northern Hemisphere land surfaces are ventilated to the free troposphere, and the rate of interhemispheric exchange in models (Patra *et al.*, 2011).

As a result of more than a decade's worth of work on understanding the apparently sluggish mixing in

TM5 as revealed by SF₆ simulations, a fault in one of the vertical mixing parameterizations of the model was discovered. When it was originally created, TM5 implemented the same planetary boundary layer (PBL) mixing and convection schemes as the parent ECMWF model. Recent comparisons between TM5, the ECMWF parent model, and radiosonde profile data show that the PBL scheme in TM5 performs similarly to that of the parent ECMWF model. The convective scheme, however, does not produce similar results in TM5 as compared to the ECMWF model.

Model Minus Observed SF₆, 2000–2008 mean by site

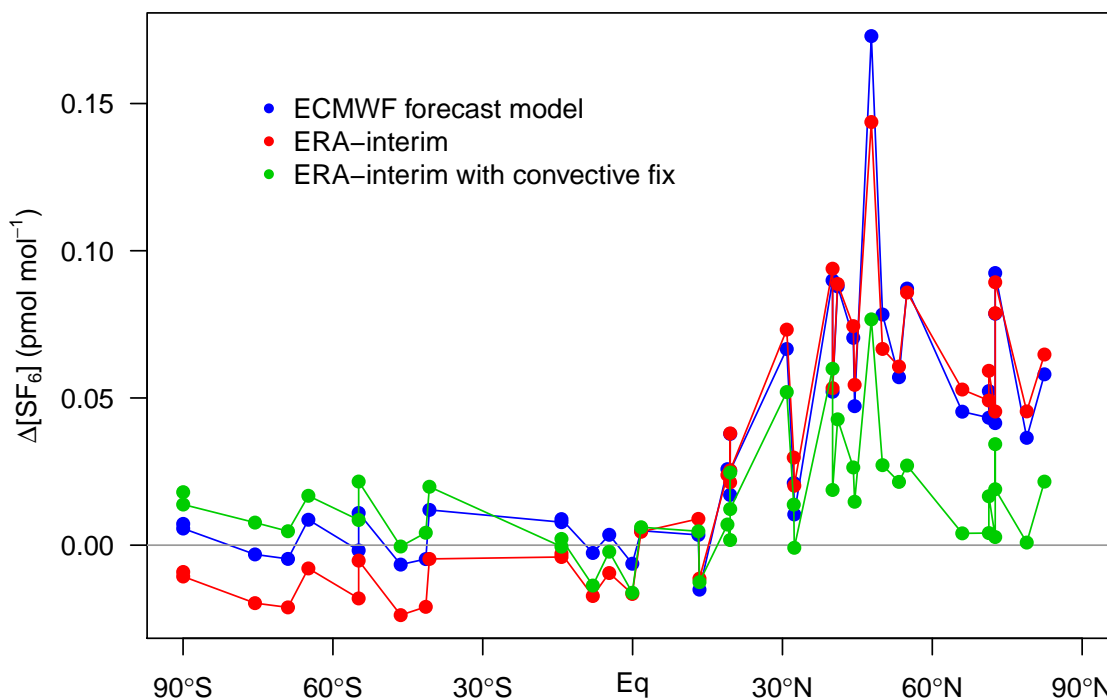


Figure 11: Long-term mean model residuals of SF₆ concentrations as a function of latitude. Residuals are defined as model-minus-observation, so a positive residual indicates the model has too much SF₆. Three different transport model simulations are shown. The ECMWF forecast (blue) and ERA-interim (red) transport simulations do not include the recent “convective flux fix”. The ERA-interim with this convective flux fix is shown in green. Units are pmol mol⁻¹, or parts per trillion. CT2015 uses the ERA-interim transport with the convective flux fix.

In a previous configuration of TM5, the convective entrainment and detrainment mass fluxes of the parent ECMWF model were re-diagnosed within TM5 using other meteorological information. The ECMWF model is used to produce both operational forecasts and the ERA-interim reanalysis, but the convective fluxes are stored for the ERA-interim product only. Thus, using ERA-interim meteorology, a direct comparison is possible. This comparison revealed that the TM5 internal re-diagnosis of convective fluxes was faulty.

TM5 was subsequently modified to directly use parent model ERA-interim convective fluxes directly. Using the parent model convective fluxes result in a significantly better SF₆ simulations. Simulations with these parent-model convective fluxes are said to use the “convective flux fix”. Simulations with the convective flux fix show significantly improved agreement with SF₆ observations (see Figure 11).

Since the parent-model convective fluxes are only available for the ERA-interim product, CT2015 uses only ERA-interim transport with the convective flux fix. Previous releases of CarbonTracker also used the ECMWF operational model transport, for which parent-model convective fluxes are not available. We believe that TM5 simulations without the parent-model convective fluxes are faulty and should not be included in be used for our product. When the convective flux fix was instituted in CT2013B, it resulted in the largest realignment of surface CO₂ fluxes in the history of the CarbonTracker program. This is a prominent example of the sensitive reliance of atmospheric inversions on accurate atmospheric transport.

6.3 References

- Krol, M., Houweling, S., Bregman, B., van den Broek, M., Segers, A., van Velthoven, P., Peters, W., Dentener, F., and Bergamaschi, P.: The two-way nested global chemistry-transport zoom model TM5: algorithm and applications, *Atmos. Chem. Phys.*, 5, 417-432, doi:10.5194/acp-5-417-2005, 2005.
- Krol, M., Houweling, S., Bregman, B., van den Broek, M., Segers, A., van Velthoven, P., Peters, W., Dentener, F., and Bergamaschi, P.: The two-way nested global chemistry-transport zoom model TM5: algorithm and applications, *Atmos. Chem. Phys.*, 5, 417-432, doi:10.5194/acp-5-417-2005, 2005.
- Denning, A. S., Holzer, Mark., Gurney, K. R., Heimann, M., Law, R. M., Rayner, P. J., Fung, I. Y., Fan, S.-M., Taguchi, S., Friedlingstein, P., Balkanski, Y., Taylor, J., Maiss, M. and Levin, I. (1999), Three-dimensional transport and concentration of SF₆. *Tellus B*, 51: 266297. doi: 10.1034/j.1600-0889.1999.00012.x
- Patra, P. K., Houweling, S., Krol, M., Bousquet, P., Belikov, D., Bergmann, D., Bian, H., Cameron-Smith, P., Chipperfield, M. P., Corbin, K., Fortems-Cheiney, A., Fraser, A., Gloor, E., Hess, P., Ito, A., Kawa, S. R., Law, R. M., Loh, Z., Maksyutov, S., Meng, L., Palmer, P. I., Prinn, R. G., Rigby, M., Saito, R., and Wilson, C.: TransCom model simulations of CH₄ and related species: linking transport, surface flux and chemical loss with CH₄ variability in the troposphere and lower stratosphere, *Atmos. Chem. Phys.*, 11, 12813-12837, doi:10.5194/acp-11-12813-2011, 2011.

- Peters, W., M. C. Krol, E. J. Dlugokencky, F. J. Dentener, P. Bergamaschi, G. Dutton, P. v. Velthoven, J. B. Miller, L. Bruhwiler, and P. P. Tans (2004), Toward regional-scale modeling using the two-way nested global model TM5: Characterization of transport using SF₆, *J. Geophys. Res.*, 109, D19314, doi:10.1029/2004JD005020

7 Observations

The observations of atmospheric CO₂ mole fraction made by NOAA ESRL and partner laboratories are at the heart of CarbonTracker. They inform us on changes in the carbon cycle, whether those changes are regular (such as the annual cycle of growth and decay of leaves and other plant matter), or irregular (such as the release of tons of carbon by a wildfire). The results in CarbonTracker depend directly on the quality, location, and frequency of available observations. The level of detail at which we can retrieve information on the carbon cycle increases strongly with the density of the CO₂ observing network.

7.1 The CarbonTracker observational network

Observations simulated by CT2015 are supplied by the GLOBALVIEW+ data product, available at the [NOAA ESRL ObsPack web site](#). This study uses measurements of air samples collected at 136 sites around the world by 32 laboratories:

- Commonwealth Scientific and Industrial Research Organization, Oceans & Atmosphere Flagship - GASLAB (CSIRO)
- Instituto de Pesquisas Energeticas e Nucleares (IPEN)
- Environment Canada (EC)
- Finnish Meteorological Institute (FMI)
- Laboratoire des Sciences du Climat et de l'Environnement - UMR8212 CEA-CNRS-UVSQ (LSCE)
- University of Heidelberg, Institut für Umweltphysik (UHEI-IUP)
- Umweltbundesamt, Station Schauinsland (UBA-SCHAU)
- Hungarian Meteorological Service (HMS)
- Center for Atmospheric and Oceanic Studies, Tohoku University (TU)
- Meteorological Research Institute (MRI)
- Japan Meteorological Agency (JMA)
- National Institute for Environmental Studies (NIES)
- Comprehensive Observation Network for TRace gases by AirLiner (CONTRAIL)
- University of Groningen (RUG), Centre for Isotope Research (CIO) (RUG)
- Energy Research Centre of the Netherlands (ECN)
- National Institute of Water and Atmospheric Research (NIWA)
- University of Science and Technology (AGH)
- South African Weather Service (SAWS)

- Izana Atmospheric Research Center, Meteorological State Agency of Spain (AEMET)
- Swiss Federal Laboratories for Materials Science and Technology (EMPA)
- World Meteorological Organization/Global Atmosphere Watch (WMO/GAW)
- University of Bern, Physics Institute, Climate and Environmental Physics (KUP)
- University of East Anglia (UEA)
- NOAA Global Monitoring Division (NOAA)
- National Center For Atmospheric Research (NCAR)
- Scripps Institution of Oceanography (SIO)
- Harvard University (HU)
- Lawrence Berkeley National Laboratory and ARM Climate Research Facility (LBNL-ARM)
- HIAPER Pole-to-Pole Observations project (HIPPO)
- University of Wisconsin (UOFWI)
- Savannah River National Laboratory (SRNL)
- Lawrence Berkeley National Laboratory (LBNL)

The data used in CarbonTracker are freely available for download from the [ESRL ObsPack web portal](#).

Two ObsPacks are available:

- The source assimilation data: the [GLOBALVIEWplus v1.0 \(2015\) ObsPack](#)
- Simulated values of the source assimilation data: the [CT2015 ObsPack](#)

Users are encouraged to review the usage requirements for these data products, and to contact the measurement laboratories directly for details about the observations.

With the advent in 2015 of GLOBALVIEW+, data are now presented to CarbonTracker with a higher temporal frequency than in past observational products. At sites with quasi-continuous monitoring, CT2015 now assimilates hourly average CO₂ concentrations. In the past, a single daily assimilation value was constructed at these sites, generally a four-hour average during well-mixed background conditions. At continental sites, this four-hour period was generally from local noon to 4pm; at many mountain sites background conditions are met at nighttime when upslope winds are rare. With GLOBALVIEW+, CarbonTracker now assimilates each hourly average during these background conditions independently.

Note that all of these observations are calibrated against the same world CO₂ standard (WMO-X2007).

At most quasi-continuous sampling sites, we assimilate only local afternoon mole fraction observations, recognizing that our atmospheric transport model does not always capture the stable planetary boundary layer over land. Daytime well-mixed conditions are much easier to match using global, coarse-resolution transport models of this class.

Starting with GLOBALVIEW+, we generally use the recommendations of data providers as to which observations are appropriate for assimilation. Such observations are identified by a variable in the ObsPack

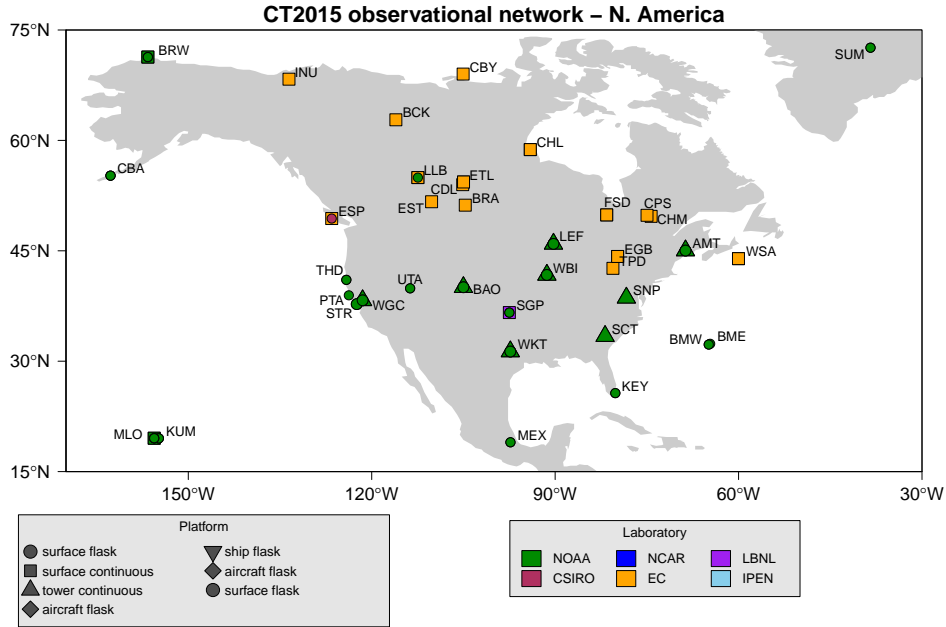


Figure 12: CarbonTracker observational network over North America. See the CarbonTracker [interactive network map](#) for more details.

distribution, obs_flag. Only observations with obs_flag = 1 are identified for assimilation by data providers. We modify the designation of assimilation data for Environment Canada quasi-continuous sampling sites. For these data, obs_flag is set to 1 by the data provider for times when they represent the daily minimum CO₂ concentration. This is generally later in the day than our standard scheme of local noon-4pm used to represent times of well-mixed PBLs. For these datasets, we have changed obs_flag to indicate assimilation only for the local noon - 4pm time period.

At mountain-top sites (*e.g.* MLO, NWR, and SPL), it is usually nighttime hours that are selected for assimilation, as these tend to be the most stable time period. Nighttime hours also avoid periods of upslope flows that contain local vegetative and/or anthropogenic influence.

Data from the Suro tower (STR_01P0) and the Boulder tower (BAO_01P0, BAO_01C3) are strongly influenced by local urban emissions, which CarbonTracker is unable to resolve. At these two sites, pollution events have been identified using co-located measurements of carbon monoxide. In this study, measurements thought to be affected by pollution events have been excluded. This technique is under active refinement.

Note that aircraft observations are *not* assimilated, but are instead retained for independent cross-validation of CarbonTracker results.

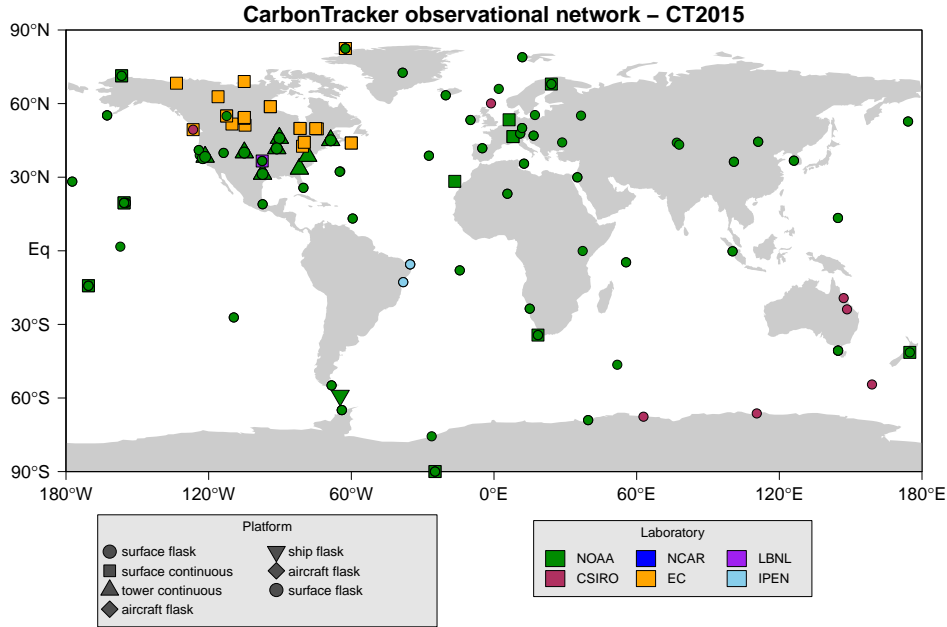


Figure 13: CarbonTracker global observational network. See the CarbonTracker [interactive network map](#) for more details.

We apply a further selection criterion during the assimilation to exclude non-marine boundary layer (MBL) observations that are very poorly forecasted in our framework. We use the so-called model-data mismatch in this process, which is the random error ascribed to each observation to account for measurement errors as well as modeling errors of that observation. We interpret an observed-minus-forecasted mole fraction that exceeds 3 times the prescribed model-data mismatch as an indicator that our modeling framework fails. This can happen for instance when an air sample is representative of local exchange not captured well by our $1^\circ \times 1^\circ$ fluxes, when local meteorological conditions are not captured by our offline transport fields, but also when large-scale CO_2 exchange is suddenly changed (*e.g.* fires, pests, droughts) to an extent that can not be accommodated by our flux modules. This last situation would imply an important change in the carbon cycle and has to be recognized by the researchers when analyzing the results. In accordance with the 3-sigma rejection criterion, about 0.2% of the observations are discarded through this mechanism in our assimilations.

7.2 Adaptive model-data mismatch

The statistical optimization method we use to constrain surface CO_2 fluxes requires that each assimilation constraint is assigned a “model-data mismatch” (MDM) error value. This is meant to express the statistics of

simulated-minus-observed CO₂ observations we could expect if CarbonTracker were using perfect surface fluxes. Such deviations arise from many sources, including random noise in the measurement system, *in situ* variability that we do not expect to resolve in our model, and faults with the atmospheric transport model. Generally, transport and inverse model faults are the dominant terms in MDM values. The MDM is one of two major “tuning knobs” used to adjust the performance of our ensemble Kalman filter. The other is also an error quantity, meant to represent the expected error on our first-guess fluxes. Discussion of this prior covariance error can be found in section 8.2.

Prior to CT2015, CarbonTracker used a single MDM value for each assimilation dataset. The NOAA continuous observations at the 396m level of the WLEF tower in northern Wisconsin, for example, were assigned a MDM of 3.0 ppm, meaning that the residuals between model-forecasted measurements and the actual observed concentrations are expected to be unbiased (*i.e.*, have a mean of zero) and have a standard deviation of 3 ppm. In practice, however, we have found that it is far easier to simulate wintertime observations than those during summer. This is mainly due to higher ambient variability of CO₂ in the summer.

With CT2015, we have started to use a new empirical scheme to assign MDM values, using statistics of model performance from a preliminary inversion. The posterior residuals for each dataset are analyzed for equally-spaced intervals of one-tenth of a year. For each of these periods, bias and random error are combined to form total deviation from observed values. The assigned MDM is set to a constant fraction (currently 80%) of this total posterior error. This scaling is meant to force the assimilation scheme to extract as much information as possible from available observations.

Our new scheme assigns observations from this dataset a variable MDM of between 1.6 ppm (in winter) and 7.9 ppm (in summer).

The adaptive MDM scheme performs well in terms of average χ^2 , which in an optimally-tuned system should be close to 1.0 for each dataset (see Table 2). Notably, the seasonal variations of MDM successfully compensate for the higher ambient variability of CO₂ at continental sites during the growing season. It is, however, an iterative process, requiring that we conduct a previous inversion. For various reasons, this previous inversion performed before CT2015 differs in significant aspects from the actual CT2015 inversions. These differences have led to MDM values which are slightly too large and thus average χ^2 values which are generally smaller than the target of 1.0 (in some cases, as low as 0.2 or 0.3). The next iteration of CarbonTracker will be able to use the more recent CT2015 inversions to refine the adaptive MDM scheme.

Duplicate observations are identified as those within 50 minutes temporally, 10m vertically, and 0.05

degrees of latitude and longitude laterally (nominally, about 5km). The MDM for such observations is inflated by \sqrt{n} , where n is the number of duplicates.

7.3 Statistical performance of CT2015

Table 2 summarizes the datasets assimilated in CarbonTracker, and the performance of the assimilation scheme at each site. These diagnostics are useful for evaluating how well CarbonTracker does in simulating observed CO₂.

Dataset	Lab.	Location	Latitude	Longitude	Elev. (m)	Used	Rej.	R (ppm)	χ^2 (ppm)	Bias (ppm)	SE (ppm)
co2-abp-surface-flask_1-representative	NOAA	Arembepe, Bahia, Brazil	12.77°S	38.17°W	1	101	0	0.6 - 2.5	0.21	-0.44	0.68
co2-abp-surface-flask_26-marine	IPEN	Arembepe, Bahia, Brazil	12.77°S	38.17°W	1	103	1	0.8 - 4.6	0.35	-0.71	1.30
co2-alt-surface-flask_1-representative	NOAA	Alert, Nunavut, Canada	82.45°N	62.51°W	200	822	1	0.4 - 2.8	0.53	0.06	0.55
co2-alt-surface-flask_2-representative	CSIRO	Alert, Nunavut, Canada	82.45°N	62.51°W	200	505	4	0.4 - 1.4	0.95	0.14	0.58
co2-alt-surface-flask_4-representative	SIO	Alert, Nunavut, Canada	82.45°N	62.51°W	200	347	1	0.4 - 2.9	0.67	0.24	0.55
co2-alt-surface-insitu_6_allvalid	EC	Alert, Nunavut, Canada	82.45°N	62.51°W	200	18070	104	0.4 - 2.5	0.76	0.06	0.60
co2-amt-surface-pfp_1-allvalid	NOAA	Argyle, Maine, United States	45.03°N	68.68°W	53	891	3	1.6 - 10.9	0.33	0.33	3.16
co2-amt-tower-insitu_1_allvalid-107magl	NOAA	Argyle, Maine, United States	45.03°N	68.68°W	53	12872	57	2.2 - 14.6	0.34	0.37	3.41
co2-ara-surface-flask_2-representative	CSIRO	Arcturus, Queensland, Australia	23.86°S	148.47°E	175	22	0	2.9 - 7.1	0.52	-0.99	3.28
co2-asc-surface-flask_1-representative	NOAA	Ascension Island, United Kingdom	7.97°S	14.40°W	85	1269	0	0.5 - 1.1	1.00	-0.03	0.66
co2-ask-surface-flask_1-representative	NOAA	Assekrem, Algeria	23.26°N	5.63°E	2710	652	3	0.6 - 1.0	0.65	-0.01	0.60
co2-azr-surface-flask_1-representative	NOAA	Terceira Island, Azores, Portugal	38.77°N	27.38°W	19	395	5	1.0 - 2.5	0.96	0.39	1.45
co2-bal-surface-flask_1-representative	NOAA	Baltic Sea, Poland	55.35°N	17.22°E	3	971	5	4.0 - 6.2	0.69	-0.96	4.11
co2-bao-surface-pfp_1-allvalid	NOAA	Boulder Atmospheric Observatory, Colorado, United States	40.05°N	105.00°W	1584	1845	4	3.1 - 21.9	0.28	-2.02	3.10
co2-bao-tower-insitu_1_allvalid-300magl	NOAA	Boulder Atmospheric Observatory, Colorado, United States	40.05°N	105.00°W	1584	8850	5	7.0 - 24.6	0.15	-2.21	3.73
co2-bck-surface-insitu_6_allvalid	EC	Behchoko, Northwest Territories, Canada	62.80°N	116.05°W	179	5460	46	0.9 - 6.3	0.84	0.24	2.29

(table continued on next page)

Dataset	Lab.	Location	Latitude	Longitude	Elev. (m)	Used	Rej.	R (ppm)	χ^2 (ppm)	Bias (ppm)	SE (ppm)
co2_bhd_surface-flask_1_representative	NOAA	Baring Head Station, New Zealand	41.41°S	174.87°E	85	196	1	0.6 - 1.3	0.76	0.08	0.57
co2_bhd_surface-insitu_15_baseline	NIWA	Baring Head Station, New Zealand	41.41°S	174.87°E	85	479	2	0.5 - 1.1	0.84	0.31	0.48
co2_bkt_surface-flask_1_representative	NOAA	Bukit Kotabang, Indonesia	0.20°S	100.32°E	845	315	4	3.7 - 5.1	0.90	2.54	3.64
co2_bme_surface-flask_1_representative	NOAA	St. Davids Head, Bermuda, United Kingdom	32.37°N	64.65°W	12	233	3	1.2 - 2.3	0.83	0.56	1.51
co2_bmw_surface-flask_1_representative	NOAA	Tudor Hill, Bermuda, United Kingdom	32.26°N	64.88°W	30	489	13	0.8 - 1.6	0.95	0.56	1.11
co2_bra_surface-insitu_6_allvalid	EC	Bratt's Lake Saskatchewan, Canada	51.20°N	104.70°W	595	5472	16	2.5 - 17.1	0.44	-0.10	3.83
co2_brw_surface-flask_1_representative	NOAA	Barrow, Alaska, United States	71.32°N	156.61°W	11	842	9	0.6 - 3.6	1.19	-0.00	0.96
co2_brw_surface-insitu_1_allvalid	NOAA	Barrow, Alaska, United States	71.32°N	156.61°W	11	11183	17	0.9 - 4.1	0.60	0.09	0.78
co2_bsc_surface-flask_1_representative	NOAA	Black Sea, Constanta, Romania	44.18°N	28.66°E	0	431	3	6.4 - 16.5	0.63	-4.66	8.53
co2_cba_surface-flask_1_representative	NOAA	Cold Bay, Alaska, United States	55.21°N	162.72°W	21	985	11	0.9 - 3.4	0.89	-0.47	1.70
co2_cba_surface-flask_4_representative	SIO	Cold Bay, Alaska, United States	55.21°N	162.72°W	21	309	4	0.5 - 4.2	0.82	-0.03	1.80
co2_cby_surface-insitu_6_allvalid	EC	Cambridge Bay, Nunavut Territory, Canada	69.01°N	105.05°W	35	2376	7	1.2 - 5.0	0.15	0.33	1.46
co2_cdl_surface-insitu_6_allvalid	EC	Candle Lake, Saskatchewan, Canada	53.99°N	105.12°W	600	11083	14	2.2 - 20.2	0.31	0.14	2.33
co2_cfa_surface-flask_2_representative	CSIRO	Cape Ferguson, Queensland, Australia	19.28°S	147.06°E	2	300	2	0.8 - 2.6	0.60	-0.37	0.99
co2_cgo_surface-flask_1_representative	NOAA	Cape Grim, Tasmania, Australia	40.68°S	144.69°E	94	517	0	0.3 - 1.1	0.84	0.02	0.27
co2_cgo_surface-flask_2_representative	CSIRO	Cape Grim, Tasmania, Australia	40.68°S	144.69°E	94	757	5	0.3 - 1.3	0.77	-0.01	0.29
co2_cgo_surface-flask_4_representative	SIO	Cape Grim, Tasmania, Australia	40.68°S	144.69°E	94	313	4	0.3 - 0.7	1.25	0.20	0.29
co2_chl_surface-insitu_6_allvalid	EC	Churchill, Manitoba, Canada	58.75°N	94.07°W	29	3279	45	0.8 - 3.6	0.82	-0.02	1.80

(table continued on next page)

Dataset	Lab.	Location	Latitude	Longitude	Elev. (m)	Used	Rej.	R (ppm)	χ^2 (ppm)	Bias (ppm)	SE (ppm)
co2_chm_surface-insitu_6_allvalid	EC	Chibougamau, Quebec, Canada	49.68°N	74.30°W	393	3728	13	2.9 - 12.1	0.28	-0.01	2.59
co2_chr_surface-flask_1_representati	NOAA	Christmas Island, Republic of Kiribati	1.70°N	157.15°W	0	501	0	0.4 - 1.1	0.48	-0.13	0.51
co2_cib_surface-flask_1_representative	NOAA	Centro de Investigacion de la Baja Atmosfera (CIBA), Spain	41.81°N	4.93°W	845	253	2	1.7 - 4.3	0.83	0.39	2.62
co2_cps_surface-insitu_6_allvalid	EC	Chapais, Quebec, Canada	49.82°N	74.98°W	381	4325	7	1.4 - 15.9	0.41	0.65	2.69
co2_cpt_surface-flask_1_representative	NOAA	Cape Point, South Africa	34.35°S	18.49°E	230	190	0	0.6 - 2.8	0.22	-0.08	0.70
co2_cpt_surface-insitu_36_marine	SAWS	Cape Point, South Africa	34.35°S	18.49°E	230	99158	149	0.6 - 1.2	0.87	0.06	0.46
co2_crz_surface-flask_1_representative	NOAA	Crozet Island, France	46.43°S	51.85°E	197	569	0	0.3 - 0.4	0.83	0.02	0.26
co2_cya_surface-flask_2_representati	CSIRO	Casey, Antarctica, Australia	66.28°S	110.52°E	47	333	0	0.3 - 0.7	0.38	-0.07	0.25
co2_drp_shipboard-flask_1_representative	NOAA	Drake Passage, N/A	59.00°S	64.69°W	0	181	1	0.3 - 0.7	0.45	0.05	0.27
co2_egb_surface-insitu_6_allvalid	EC	Egbert, Ontario, Canada	44.23°N	79.78°W	251	9380	56	4.2 - 19.7	0.25	-0.98	4.35
co2_eic_surface-flask_1_representative	NOAA	Easter Island, Chile	27.16°S	109.43°W	47	443	4	0.8 - 1.2	1.13	0.51	1.01
co2_esp_surface-flask_2_representati	CSIRO	Estevan Point, British Columbia, Canada	49.38°N	126.54°W	7	23	0	0.3 - 5.0	0.83	-0.65	1.18
co2_esp_surface-insitu_6_allvalid	EC	Estevan Point, British Columbia, Canada	49.38°N	126.54°W	7	5482	54	1.8 - 7.4	0.51	0.00	2.44
co2_est_surface-insitu_6_allvalid	EC	Esther, Alberta, Canada	51.66°N	110.21°W	707	4850	27	2.3 - 16.1	0.30	0.04	3.03
co2_etl_surface-insitu_6_allvalid	EC	East Trout Lake, Saskatchewan, Canada	54.35°N	104.98°W	492	12421	33	1.4 - 6.9	0.51	0.11	2.06
co2_fsd_surface-insitu_6_allvalid	EC	Fraserdale, Canada	49.88°N	81.57°W	210	18948	51	1.7 - 12.8	0.34	0.22	2.56
co2_gmi_surface-flask_1_representative	NOAA	Mariana Islands, Guam	13.39°N	144.66°E	0	903	21	0.7 - 1.1	0.76	0.14	0.77

(table continued on next page)

Dataset	Lab.	Location	Latitude	Longitude	Elev. (m)	Used	Rej.	R (ppm)	χ^2 (ppm)	Bias (ppm)	SE (ppm)
co2_hba_surface-flask_1_representati	NOAA	Halley Station, Antarctica, United Kingdom	75.61°S	26.21°W	30	647	0	0.2 - 0.4	0.66	0.08	0.18
co2_hpb_surface-flask_1_representative	NOAA	Hohenpeissenberg, Germany	47.80°N	11.02°E	936	379	0	3.9 - 9.2	0.86	1.53	5.33
co2_hun_surface-flask_1_representati	NOAA	Hegyhals, Hungary	46.95°N	16.65°E	248	699	3	3.2 - 8.5	0.59	-1.07	4.24
co2_ice_surface-flask_1_representative	NOAA	Storhofdi, Vestmannaeyjar, Iceland	63.40°N	20.29°W	118	639	17	1.0 - 1.6	0.88	-0.59	1.34
co2_inu_surface-insitu_6_allvalid	EC	Inuvik, Northwest Territories, Canada	68.32°N	133.53°W	113	3074	18	0.8 - 5.7	0.98	0.24	2.02
co2_izo_surface-insitu_27_allvalid	AEMET	Izana, Tenerife, Canary Islands, Spain	28.31°N	16.50°W	2373	56436	212	0.9 - 1.4	0.57	0.17	0.74
co2_jfj_surface-insitu_49_allvalid	KUP	Jungfraujoch, Switzerland	46.55°N	7.99°E	3570	12027	118	1.8 - 4.4	0.56	0.20	1.99
co2_jfj_surface-insitu_5_allvalid	EMPA	Jungfraujoch, Switzerland	46.55°N	7.99°E	3570	5237	29	1.5 - 4.1	0.40	0.17	1.86
co2_key_surface-flask_1_representati	NOAA	Key Biscayne, Florida, United States	25.67°N	80.16°W	1	491	7	1.0 - 2.1	0.70	0.45	1.39
co2_kum_surface-flask_1_representative	NOAA	Cape Kumukahi, Hawaii, United States	19.52°N	154.82°W	3	895	7	0.8 - 2.6	0.62	-0.12	0.98
co2_kum_surface-flask_4_representati	SIO	Cape Kumukahi, Hawaii, United States	19.52°N	154.82°W	3	499	8	0.8 - 2.7	0.55	-0.05	1.15
co2_kzd_surface-flask_1_representative	NOAA	Sary Taukum, Kazakhstan	44.08°N	76.87°E	595	438	3	1.5 - 3.1	0.79	-0.50	2.12
co2_kzm_surface-flask_1_representati	NOAA	Plateau Assy, Kazakhstan	43.25°N	77.88°E	2519	389	4	1.6 - 4.0	0.86	-0.04	2.32
co2_lef_surface-pfp_1_allvalid	NOAA	Park Falls, Wisconsin, United States	45.95°N	90.27°W	472	1648	5	1.8 - 10.8	0.41	-0.22	2.74
co2_lef_tower-insitu_1_allvalid-396magl	NOAA	Park Falls, Wisconsin, United States	45.95°N	90.27°W	472	18997	192	1.6 - 7.9	0.64	0.01	2.57
co2_llb_surface-flask_1_representative	NOAA	Lac La Biche, Alberta, Canada	54.95°N	112.45°W	540	155	4	2.3 - 11.3	0.52	-0.48	3.80
co2_llb_surface-insitu_6_allvalid	EC	Lac La Biche, Alberta, Canada	54.95°N	112.45°W	540	9801	21	5.0 - 40.5	0.18	0.16	4.19

(table continued on next page)

Dataset	Lab.	Location	Latitude	Longitude	Elev. (m)	Used	Rej.	R (ppm)	χ^2 (ppm)	Bias (ppm)	SE (ppm)
co2_imp_surface-flask_1_representative	NOAA	Lampedusa, Italy	35.52°N	12.62°E	45	333	4	1.2 - 1.9	0.85	0.10	1.33
co2_lut_surface-insitu_44_allvalid	RUG	Lutjewad, Netherlands	53.40°N	6.35°E	1	8591	90	5.2 - 10.3	0.48	-1.16	5.38
co2_maa_surface-flask_2_representative	CSIRO	Mawson Station, Antarctica, Australia	67.62°S	62.87°E	32	356	0	0.3 - 0.7	0.38	-0.05	0.25
co2_mex_surface-flask_1_representati	NOAA	High Altitude Global Climate Observation Center, Mexico	18.98°N	97.31°W	4464	242	0	0.9 - 2.9	0.96	0.96	1.53
co2_mhd_surface-flask_1_representative	NOAA	Mace Head, County Galway, Ireland	53.33°N	9.90°W	5	581	4	0.8 - 1.6	0.64	0.08	0.95
co2_mid_surface-flask_1_representati	NOAA	Sand Island, Midway, United States	28.21°N	177.38°W	11	680	6	0.8 - 1.5	1.01	0.49	0.98
co2_mkn_surface-flask_1_representative	NOAA	Mt. Kenya, Kenya	0.06°S	37.30°E	3644	137	1	1.3 - 3.1	1.14	1.71	1.87
co2_mlo_surface-flask_1_representati	NOAA	Mauna Loa, Hawaii, United States	19.54°N	155.58°W	3397	1084	6	0.4 - 1.2	0.87	0.17	0.52
co2_mlo_surface-flask_2_representative	CSIRO	Mauna Loa, Hawaii, United States	19.54°N	155.58°W	3397	483	0	0.4 - 1.7	0.78	0.25	0.58
co2_mlo_surface-flask_4_representati	SIO	Mauna Loa, Hawaii, United States	19.54°N	155.58°W	3397	552	6	0.5 - 1.3	0.96	0.35	0.57
co2_mlo_surface-insitu_1_allvalid	NOAA	Mauna Loa, Hawaii, United States	19.54°N	155.58°W	3397	14714	0	0.6 - 1.2	0.55	0.22	0.45
co2_mqa_surface-flask_2_representati	CSIRO	Macquarie Island, Australia	54.48°S	158.97°E	6	440	0	0.3 - 0.7	0.49	-0.00	0.29
co2_nat_surface-flask_1_representative	NOAA	Maxaranguape, Brazil	5.51°S	35.26°W	15	171	0	0.9 - 3.1	0.44	-0.61	0.96
co2_nat_surface-flask_26_marine	IPEN	Maxaranguape, Brazil	5.51°S	35.26°W	15	89	0	0.7 - 3.1	0.44	-0.42	1.05
co2_nmb_surface-flask_1_representative	NOAA	Gobabeb, Namibia	23.58°S	15.03°E	456	295	0	0.5 - 1.4	0.60	-0.19	0.82
co2_obn_surface-flask_1_representati	NOAA	Obrninsk, Russia	55.11°N	36.60°E	183	133	0	3.9 - 10.2	0.50	0.19	4.34
co2_oxk_surface-flask_1_representative	NOAA	Ochsenkopf, Germany	50.03°N	11.81°E	1009	316	3	2.9 - 4.9	0.87	-0.54	3.65

(table continued on next page)

Dataset	Lab.	Location	Latitude	Longitude	Elev. (m)	Used	Rej.	R (ppm)	χ^2 (ppm)	Bias (ppm)	SE (ppm)
co2_pal_surface-flask_1_representati	NOAA	Pallas-Sammaltunturi, GAW Station, Finland	67.97°N	24.12°E	560	536	5	1.4 - 6.7	0.67	-0.29	2.19
co2_pal_surface-insitu_30_marine	FMI	Pallas-Sammaltunturi, GAW Station, Finland	67.97°N	24.12°E	560	22507	46	0.8 - 3.1	0.61	0.05	0.79
co2_poc_shipboard-flask_1_representati	NOAA	Pacific Ocean, N/A			0	2134	28	0.6 - 2.6	0.49	0.00	0.71
co2_psa_surface-flask_1_representative	NOAA	Palmer Station, Antarctica, United States	64.92°S	64.00°W	10	722	0	0.3 - 0.8	0.40	-0.02	0.23
co2_psa_surface-flask_4_representati	SIO	Palmer Station, Antarctica, United States	64.92°S	64.00°W	10	346	3	0.2 - 0.6	0.77	0.14	0.21
co2_pta_surface-flask_1_representative	NOAA	Point Arena, California, United States	38.95°N	123.74°W	17	387	11	3.2 - 6.7	0.70	-0.70	4.25
co2_rpb_surface-flask_1_representati	NOAA	Ragged Point, Barbados	13.16°N	59.43°W	15	686	4	0.8 - 1.1	0.57	0.11	0.64
co2_sct_tower-insitu_1_allvalid_305magl	NOAA	Beech Island, South Carolina, United States	33.41°N	81.83°W	115	8534	64	3.8 - 7.3	0.54	-0.84	3.80
co2_sey_surface-flask_1_representati	NOAA	Mahe Island, Seychelles	4.68°S	55.53°E	2	643	0	0.5 - 1.3	1.05	0.00	0.77
co2_sgp_surface-flask_1_representative	NOAA	Southern Great Plains, Oklahoma, United States	36.61°N	97.49°W	314	577	7	2.0 - 9.3	0.84	-0.93	3.33
co2_sgp_surface-insitu_64_allvalid_60magl	LBNL-ARM	Southern Great Plains, Oklahoma, United States	36.61°N	97.49°W	314	13350	21	3.4 - 17.4	0.29	-0.29	3.35
co2_shm_surface-flask_1_representative	NOAA	Shemya Island, Alaska, United States	52.71°N	174.13°E	23	489	3	0.8 - 3.7	0.89	-0.18	1.99
co2_sis_surface-flask_2_representati	CSIRO	Shetland Islands, Scotland	60.09°N	1.25°W	30	89	0	0.6 - 2.1	0.67	0.54	0.93
co2_smo_surface-flask_1_representative	NOAA	Tutuila, American Samoa	14.25°S	170.56°W	42	1155	3	0.3 - 3.1	0.57	-0.06	0.48
co2_smo_surface-flask_4_representati	SIO	Tutuila, American Samoa	14.25°S	170.56°W	42	406	1	0.4 - 4.6	0.54	0.02	0.68
co2_smo_surface-insitu_1_allvalid	NOAA	Tutuila, American Samoa	14.25°S	170.56°W	42	15361	0	0.4 - 3.4	0.24	-0.00	0.41

(table continued on next page)

Dataset	Lab.	Location	Latitude	Longitude	Elev. (m)	Used	Rej.	R (ppm)	χ^2 (ppm)	Bias (ppm)	SE (ppm)
co2_snp_tower-insitu_1_allvalid-17magl	NOAA	Shenandoah National Park, United States	38.62°N	78.35°W	1008	7381	133	2.5 - 6.5	0.91	0.53	4.95
co2_spo_surface-flask_1_representative	NOAA	South Pole, Antarctica, United States	89.98°S	24.80°W	2810	772	0	0.2 - 1.3	0.55	0.10	0.19
co2_spo_surface-flask_4_representati	SIO	South Pole, Antarctica, United States	89.98°S	24.80°W	2810	346	0	0.2 - 1.2	0.69	0.12	0.20
co2_spo_surface-insitu_1_allvalid	NOAA	South Pole, Antarctica, United States	89.98°S	24.80°W	2810	20068	2	0.2 - 1.3	0.50	0.02	0.16
co2_stm_surface-flask_1_representati	NOAA	Ocean Station M, Norway	66.00°N	2.00°E	0	844	8	0.7 - 2.0	0.65	0.12	0.94
co2_str_surface-pfp_1_allvalid	NOAA	Sutro Tower, San Francisco, California, United States	37.76°N	122.45°W	254	1361	25	1.9 - 4.0	0.76	-0.49	2.65
co2_sum_surface-flask_1_representati	NOAA	Summit, Greenland	72.60°N	38.42°W	3210	613	11	0.5 - 1.0	0.90	0.14	0.73
co2_syo_surface-flask_1_representative	NOAA	Syowa Station, Antarctica, Japan	69.01°S	39.59°E	14	347	0	0.2 - 0.4	0.42	-0.03	0.20
co2_tap_surface-flask_1_representati	NOAA	Tae-ahn Peninsula, Republic of Korea	36.74°N	126.13°E	16	591	6	2.6 - 6.6	0.67	-0.28	2.92
co2_thd_surface-flask_1_representative	NOAA	Trinidad Head, California, United States	41.05°N	124.15°W	107	549	16	2.1 - 5.8	0.81	-1.13	4.06
co2_ush_surface-flask_1_representati	NOAA	Ushuaia, Argentina	54.85°S	68.31°W	12	351	0	0.6 - 1.0	0.66	-0.36	0.49
co2_uta_surface-flask_1_representative	NOAA	Wendover, Utah, United States	39.90°N	113.72°W	1327	641	8	1.1 - 2.5	0.80	0.37	1.70
co2_uum_surface-flask_1_representati	NOAA	Ulaan Uul, Mongolia	44.45°N	111.10°E	1007	665	25	1.9 - 3.6	0.91	-0.47	3.43
co2_wbi_surface-pfp_1_allvalid	NOAA	West Branch, Iowa, United States	41.72°N	91.35°W	242	1740	5	2.8 - 19.8	0.40	-0.76	4.16
co2_wbi_tower-insitu_1_allvalid-379magl	NOAA	West Branch, Iowa, United States	41.72°N	91.35°W	242	9548	74	3.0 - 12.8	0.59	-0.43	3.98
co2_wgc_surface-pfp_1_allvalid	NOAA	Walnut Grove, California, United States	38.27°N	121.49°W	0	1372	5	6.4 - 27.0	0.42	-2.44	7.10

(table continued on next page)

Dataset	Lab.	Location	Latitude	Longitude	Elev. (m)	Used	Rej.	R (ppm)	χ^2 (ppm)	Bias (ppm)	SE (ppm)
co2_wgc_tower-insitu_1_allvalid-483magl	NOAA	Walnut Grove, California, United States	38.27°N	121.49°W	0	9455	115	4.6 - 8.6	0.58	-0.27	4.75
co2_wis_surface-flask_1_representative	NOAA	WIS Station, Negev Desert, Israel	29.97°N	35.06°E	151	732	6	1.4 - 3.4	0.80	-0.29	1.98
co2_wkt_surface-pfp_1_allvalid	NOAA	Moody, Texas, States	31.31°N	97.33°W	251	1774	7	2.2 - 11.6	0.39	-0.53	2.47
co2_wkt_tower-insitu_1_allvalid-457magl	NOAA	Moody, Texas, States	31.31°N	97.33°W	251	14627	160	2.7 - 8.2	0.58	-0.29	2.57
co2_wlg_surface-flask_1_representati	NOAA	Mt. Waliguan, Peoples Republic of China	36.29°N	100.90°E	3810	570	18	1.1 - 2.0	0.85	0.00	1.46
co2_wsa_surface-insitu_6_allvalid	EC	Sable Island, Nova Scotia, Canada	43.93°N	60.02°W	5	14272	235	1.6 - 3.5	0.67	-0.05	2.21
co2_zep_surface-flask_1_representati	NOAA	Ny-Alesund, Svalbard, Norway and Sweden	78.91°N	11.89°E	474	749	8	0.7 - 1.4	0.79	0.16	0.85

Table 2: Summary of Observational Sites Used in CarbonTracker. The site location is specified by latitude, longitude and elevation in meters above sea level. The number of observations actually assimilated for each dataset is listed in the column “Used”, and the number rejected due to inability to fit the observations is listed in the column “Rej.”. Model-data-mismatch (R) is a value assigned to a given site that is meant to quantify our expected ability to simulate observations there. In this table we report the range of R values assigned to dataset observations by our “adaptive” model-data mismatch scheme (Sec. 7.2). These values are principally determined from the limitations of the atmospheric transport model. It is part of the standard deviation used to interpret the difference between a simulation first guess (Hx) of an observation and the actual measured value (z). The other component, HPH^T , is a measure of the ability of the ensemble Kalman filter to improve its simulated value for this observation by adjusting fluxes. These elements together form the innovation χ statistic for the site: $\chi = (z - Hx) / \sqrt{(HPH^T + R^2)}$. The innovation χ^2 reported above is the mean of all squared χ values for a given site. An average χ^2 below 1.0 indicates that the $HPH^T + R^2$ values are too large. Conversely, values above 1.0 mean that this standard deviation is underestimated. The bias and SE columns are statistics of the posterior residuals (final modeled values - measured values). The bias is the mean of these residuals; the SE is the standard error of those residuals.

7.4 References

- [ESRL Carbon Cycle Program](#)
- [WMO/GAW Report No. 168, 2006](#)

8 Ensemble data assimilation

Data assimilation is the process by which a model simulation is adjusted to agree with observations. Model simulations may drift off from reality for a number of reasons. Some models are highly nonlinear, and depend sensitively on knowing the system state with high accuracy. Weather models fall into this category, and as a result reliable forecast systems depend on having a constant stream of meteorological data to correct their simulations. In contrast, models like CarbonTracker need data assimilation not because the controlling dynamics are nonlinear, but because those dynamics are not well known. CarbonTracker uses approximate or estimated rules about the evolution of surface CO₂ fluxes, then corrects these approximate projections using observational constraints. The resulting optimal surface flux estimates can then be used to better understand the functioning of the carbon cycle.

Data assimilation is usually a cyclical process, in which estimates get refined over time as more observations become available. Mathematically, data assimilation can be performed using a wide variety of techniques, including variational and ensemble methods. Assimilation systems involving simulations of the global atmosphere are often implemented on highly parallel supercomputers in order to distribute the workload among many computational cores. CarbonTracker is an example of such a model because it relies heavily on estimates of global atmospheric transport.

CarbonTracker model predictions are mainly limited by the relatively simple representations of CO₂ surface exchange used to predict land biosphere and ocean fluxes and emissions from fossil fuel combustion and wildfires. As described in the following section, we use data assimilation techniques to modify these surface fluxes so that the resulting atmospheric distribution of CO₂ agrees optimally with measurements. We do this by estimating a set of spatially- and temporally-varying scaling factors that multiply first-guess predictions from prior flux models. Data assimilation allows us to determine optimal values for these scaling factors.

8.1 Parameterization of unknowns

Four prior flux models drive instantaneous CO₂ fluxes $F(x, y, t)$ in CarbonTracker according to

$$F(x, y, t) = \lambda(x, y, t) \left(F_{\text{land}}(x, y, t) + F_{\text{ocean}}(x, y, t) \right) + F_{\text{FF}}(x, y, t) + F_{\text{fire}}(x, y, t), \quad (11)$$

where F_{land} , F_{ocean} , F_{FF} , and F_{bio} are prior flux model predictions for land biosphere, ocean, fossil fuel and wildfire emissions respectively, and λ represents a set of unknown multiplicative scaling factors applied to the fluxes, to be estimated in the assimilation. These scaling factors are the final product of our assimilation and together with the prior flux models determine CarbonTracker optimized fluxes. Note that no scaling factors are applied to the fossil fuel and fire modules. The fossil fuel and wildfire fluxes are relatively well-known from prior flux models compared to highly-uncertain land biosphere and ocean fluxes, and as a result we impose those emissions without modification in our model.

8.1.1 Optimization regions

The scaling factors λ are estimated independently for each week and optimization region. They are assumed to be constant over this time period and spatial domain. Each scaling factor is associated with a particular region of the globe, as in the TransCom inversion study (*e.g.* Gurney *et al.*, 2002). Currently the geographic distribution of these optimization regions is fixed. The choice of regions is a strong *a priori* design decision determining the reliability of the resulting fluxes. In particular, the scale of optimization regions is chosen to minimize “aggregation errors” (Kaminski *et al.*, 2001), while limiting the set of unknown parameters to a manageable number. Following Jacobson *et al.* (2007), we have divide the global ocean into 30 basins encompassing large-scale ocean circulation and biogeochemical features. The terrestrial biosphere is divided up according to ecosystem type and geographical domain. Specifically, each of the 11 TransCom land regions is subdivided into a maximum of 19 “ecoregions” according to its [Olson \(1992\) vegetation classification](#). The set of ecoregions over North America is summarized in Table 3 and Figure 17. Note that there is currently no requirement for ecoregions to be contiguous, and a single scaling factor can be applied to the same vegetation type on both sides of a continent. Further details on ecoregions can be found in Section 9

Theoretically, this approach leads to a total number of $11 \times 19 + 30 = 239$ optimizable scaling factors for each week, but the actual number of optimization regions is only 156 since some ecosystem types are not represented in every TransCom region. It should be noted also that we have chosen to not optimize scaling

category	Olson V 1.3	Percentage area
1	Conifer Forest	19.0%
2	Broadleaf Forest	1.3%
3	Mixed Forest	7.5%
4	Grass/Shrub	12.6%
5	Tropical Forest	0.3%
6	Scrub/Woods	2.1%
7	Semitundra	19.4%
8	Fields/Woods/Savanna	4.9%
9	Northern Taiga	8.1%
10	Forest/Field	6.3%
11	Wetland	1.7%
12	Deserts	0.1%
13	Shrub/Tree/Suc	0.1%
14	Crops	9.7%
15	Conifer Snowy/Coastal	0.4%
16	Wooded tundra	1.7%
17	Mangrove	0.0%
18	Non-optimized areas (ice, polar desert, inland seas)	0.0%
19	Water	4.9%

Table 3: Ecosystem types over North America

factors for ice-covered regions, inland water bodies, and deserts, since the CO₂ flux from these regions is negligible.

It is important to note that even though only one parameter is available to scale, for instance, the flux from coniferous forests in Boreal North America, each 1° × 1° grid box predominantly covered by coniferous forests will have a different optimized flux $\lambda F_{\text{land}}(x, y, t)$ depending on local temperature, radiation, and emissions as simulated by the prior flux model.

Ecosystem types are based on the vegetation classification of [Olson, \(1992\)](#). Note that we have adjusted the original 29 categories into only 19 regions. This was done mainly to fill the unused categories 16, 17, and 18, and to group the similar categories 23-26+29. [Table 3](#) shows each vegetation category considered. Percentages indicate the relative area in North America associated with each category.

Each 1° × 1° pixel of our domain was assigned one of the categories above based on the Olson category that was most prevalent in the 0.5° × 0.5° underlying area.

8.1.2 Ensemble size and localization

The ensemble system used to solve for the scalar multiplication factors is similar to that in Peters *et al.* (2005) and based on the square root ensemble Kalman filter of Whitaker and Hamill (2002). We have restricted the length of the smoother window to only five weeks as we found the derived flux patterns within North America to be robustly resolved well within that time. We caution users of CarbonTracker results that although North American flux estimates have been determined to be robust after five weeks, regions of the world with less dense observational coverage (the tropics, Southern Hemisphere, and parts of Asia) are likely to be poorly observable even after more than a month of transport and therefore less robustly resolved. Although longer assimilation windows, or long prior covariance length-scales, could potentially help to constrain larger scale emission totals from such areas, we focus our analysis here on a region more directly constrained by atmospheric observations.

Ensemble statistics are created from 150 ensemble members, each with its own background CO₂ concentration field to represent the time history (and thus covariances) of the filter. Approximation of the covariance matrix by a discrete ensemble can result in apparent improvements in modeled measurements from fluxes that are unphysically remote. To dampen such spurious correlations, we apply localization (Houtekamer and Mitchell, 1998) for certain datasets. Localization is not used for datasets judged to represent hemisphere-scale signals, such as those from marine boundary layer sites in remote locations.

Localization ensures that datasets of continental observations within North America do not determine, for example, tropical African fluxes, unless a very robust signal is found. In contrast, marine boundary layer datasets with a known large footprint and strong capacity to see integrated flux signals are not localized. Localization is based on the linear correlation coefficient between the 150 parameter deviations and 150 observation deviations for each parameter. If the relationship between a parameter deviation and its modeled observational impact is statistically significant, then that relationship is used to modify parameters. Otherwise, the relationship is assumed to be spurious noise due to the numerical approximation of the covariance matrix by the limited ensemble. We accept relationships that reach 95% significance in a Student's T-test with a two-tailed probability distribution.

8.1.3 Dynamical model

In CarbonTracker, the dynamical model is applied to the ensemble-mean parameter values λ as:

$$\lambda^-[t] = (\lambda_0^- + \lambda^+[t-1] + \lambda^+[t-2])/3 \quad (12)$$

Where $\lambda^-[t]$ is the prior value of the scaling factors for timestep t , λ_0^- is the initial prior vector with all elements set to 1.0, and $\lambda^+[t-1]$ and $\lambda^+[t-2]$ are the posterior (“analyzed”) scaling factors for timesteps $t-1$ and $t-2$ respectively. This model describes that parameter values λ for a new time step are chosen as a combination of optimized values from the two previous time steps and a fixed overall prior value of 1.0. This operation is similar to the simple persistence forecast used in Peters *et al.* (2005), but represents a smoothing over three time steps, which attenuates variations in the forecast of λ in time. The inclusion of the prior term λ_0^- acts as a regularization (Baker *et al.*, 2006) and ensures that the parameters in our system will eventually revert back to predetermined prior values when there is no information coming from observations. Note that our dynamical model equation does not include an error term on the dynamical model, for the simple reason that we don’t know the error of this model. This is reflected in the treatment of covariance, which is always set to a fixed prior covariance structure and not forecast with our dynamical model.

8.2 Covariance structure

The prior covariance structure P_0^- describes the magnitude of the uncertainty on each parameter, plus their correlation in space. The latter is applied such that correlations between the same ecosystem types in different TransCom regions decrease exponentially with distance ($L=2000\text{km}$), and thus assumes a coupling *between* the behavior of the same ecosystems in close proximity to one another (such as coniferous forests in Boreal and Temperate North America). Furthermore, all ecosystems *within* tropical TransCom regions are coupled decreasing exponentially with distance since we do not believe the current observing network can constrain tropical fluxes on sub-continental scales, and want to prevent spurious compensating source/sink pairs (“dipoles”) to occur in the tropics.

In our standard assimilation, the chosen standard deviation is 80% on land parameters. All parameters have the same variance within the land or ocean domain. Because the parameters multiply the net-flux though, ecosystems with larger weekly mean net fluxes have a larger variance in absolute flux magnitude.

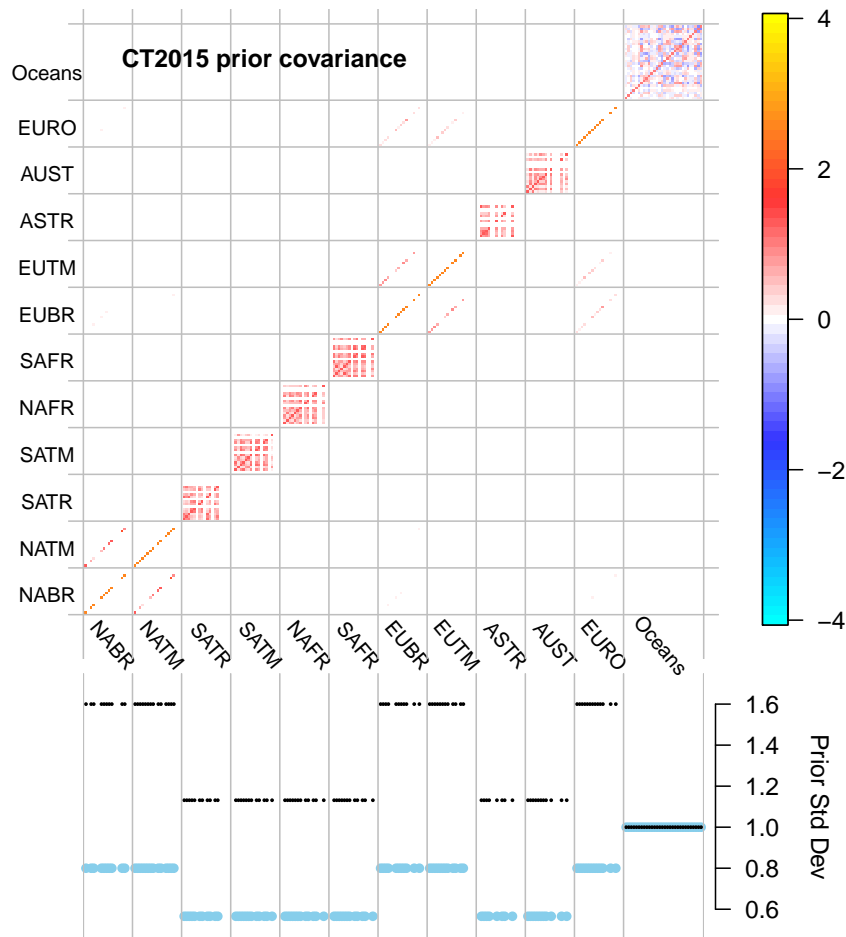
8.3 Multiple prior models

In Bayesian estimation systems like CarbonTracker, there is a potential for bias from a flux prior to propagate through the inversion system to the final result. It is difficult to quantify this effect, and as a result it is generally considered a requirement that flux priors be unbiased. We cannot guarantee this for any of our prior fluxes, be they the prior estimates for terrestrial or oceanic exchange, or the presumed wildfire and fossil fuel emissions. In order to explicitly quantify the impact of prior bias on our solution, in CT2015 we present the result of a multi-model prior suite of inversions. We have used two terrestrial flux priors (including two wildfire emissions estimates), two air-sea CO₂ exchange priors, and two estimates of imposed fossil fuel emissions in a factorial design experiment. For each of the resulting eight unique combinations of prior fluxes, we conduct an independent inversion conducted independently according to the methods described above. We present as a final result the mean flux across this suite of inversions and the atmospheric CO₂ distribution resulting from applying these mean fluxes to our atmospheric transport model. Each of the priors is described in detail in its corresponding documentation section.

8.3.1 Posterior uncertainties in CarbonTracker

The formal “internal” error estimates produced by CarbonTracker are unrealistically large. This is largely a result of the relatively short assimilation window in CarbonTracker, along with a dynamical model that introduces a fresh prior covariance matrix with every new week entering the assimilation window. This five-week window effectively inhibits the formation of anticorrelations (“dipoles”) in flux estimates, and does little to reduce the confidence interval on prior fluxes.

The temporal truncation in CarbonTracker imposed by its five-week assimilation window tends to yield regional flux estimates that are largely uncorrelated with those from other regions. A consequence of this feature is that uncertainties in CarbonTracker tend to increase as larger regions are considered; regional errors mostly just add in quadrature without any cancellation from dipole anticorrelation. Whereas many inversions yield smaller errors as the spatial extent of the region being considered increases, CarbonTracker acts in the opposite fashion. This is perhaps most obvious in the estimate of CarbonTracker’s global annual surface flux of carbon dioxide. While CT2015 estimates a one-sigma error of more than 6 PgC yr⁻¹ on its global flux, this quantity is in actuality much more well-constrained. This is evident from CarbonTracker’s excellent agreement with observational estimates of atmospheric growth rate.



• Recent, including CT2015 • Older, CT2007B–CT2010

Figure 14: CT2015 prior covariance structure. The prior covariance matrix (top panel) and the square root of diagonal members of this matrix (bottom panel). Covariance matrix quantities are dimensionless squared scaling factors, and the bottom panel is the square root of this. TransCom land regions form the first 11 large divisions on the axes here. As described above, each of those regions contains 19 potential ecosystems. Correlations between similar ecosystems in proximate TransCom regions are visible in North America (*e.g.* NABR and NATM, the boreal and temperate North American regions) and Eurasia. Within tropical TransCom regions, however, differing ecosystems are assigned a non-zero prior covariance, which is visible here as red block-like structures on the diagonal within, for example, the South America Tropical (SATR) TransCom region. Ocean regions have a more complicated covariance structure that depends on which prior is used; the structure shown here is that of the ocean inversion flux prior. The lower panel of this diagram compares the on-diagonal elements of the prior covariance matrix by plotting their square roots. The resulting standard deviations are directly comparable to the percentages discussed in section 3 above; 0.8 is equivalent to 80%. The retuning of the covariance matrix for CT2015’s multiple-prior simulation is made evident by also showing these values from previous CarbonTracker releases in light blue.

In CT2015, error estimates are about a factor of two larger than in previous releases, mainly due to the retuning of the land prior covariance discussed above. However, uncertainties presented for CT2015 take into account not only the “internal” flux uncertainty generated by a single inversion, but also the across-model “external” uncertainty representing the spread of the inversion models due to the choice of prior flux.

8.4 References

- Jeffrey S. Whitaker and Thomas M. Hamill, 2002: Ensemble Data Assimilation without Perturbed Observations. *Mon. Wea. Rev.*, 130, 1913-1924.
doi: [http://dx.doi.org/10.1175/1520-0493\(2002\)130;1913:EDAWPO;2.0.CO;2](http://dx.doi.org/10.1175/1520-0493(2002)130;1913:EDAWPO;2.0.CO;2)
- Peters, W., M. C. Krol, E. J. Dlugokencky, F. J. Dentener, P. Bergamaschi, G. Dutton, P. v. Velthoven, J. B. Miller, L. Bruhwiler, and P. P. Tans (2004), Toward regional-scale modeling using the two-way nested global model TM5: Characterization of transport using SF₆, *J. Geophys. Res.*, 109, D19314, doi:10.1029/2004JD005020
- Olson ecosystem types
- Kaminski, T., P. J. Rayner, M. Heimann, and I. G. Enting (2001), On aggregation errors in atmospheric transport inversions, *J. Geophys. Res.*, 106(D5), 4703-4715, doi:10.1029/2000JD900581.

9 Ecoregions in CarbonTracker

9.1 What are ecoregions?

Ecoregions are the actual scale on which CarbonTracker performs its optimization over land. Ecoregions are meant to represent large expanses of land within a given continent having similar ecosystem types, and are used to divide continent-scale regions into smaller domains for analysis. The ecosystem types used in CarbonTracker are derived from the [Olson \(1992\) vegetation classification](#) (Table 4, Figure 15).

We define an ecoregion as an ecosystem type within a given TransCom land region. There are 11 such TransCom land regions (Figure 16), so there are $11 \times 19 = 209$ possible ecoregions. However, not all ecosystem types are present in all TransCom regions, and the actual number of land ecoregions ends up being 126.

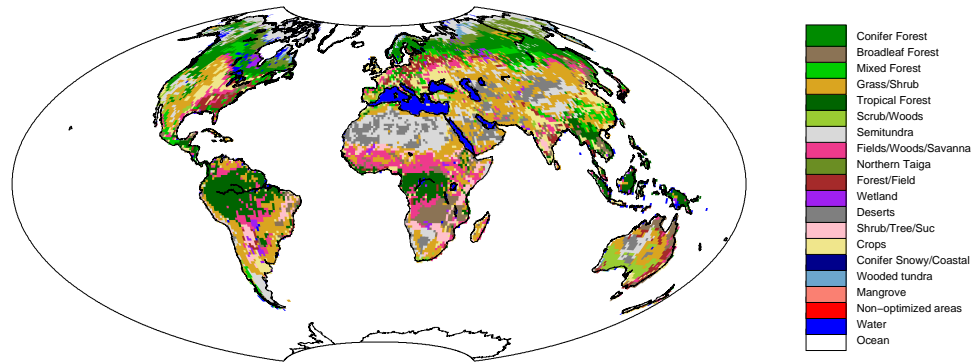


Figure 15: Global distribution of Olson ecosystem types.

Ecosystem Type	North American Boreal		North American Temperate	
	Area (km ²)	Percentage	Area (km ²)	Percentage
Conifer Forest	2315376	22.9%	1607291	14.0%
Broadleaf Forest	-	-	269838	2.4%
Mixed Forest	592291	5.9%	930813	8.1%
Grass/Shrub	53082	0.5%	2515582	21.9%
Tropical Forest	-	-	58401	0.5%
Scrub/Woods	-	-	416520	3.6%
Semitundra	3396292	33.6%	866468	7.6%
Fields/Woods/Savanna	29243	0.3%	1020939	8.9%
Northern Taiga	1658773	16.4%	-	-
Forest/Field	61882	0.6%	1243174	10.8%
Wetland	322485	3.2%	66968	0.6%
Deserts	-	-	21934	0.2%
Shrub/Tree/Suc	-	-	11339	0.1%
Crops	-	-	1969912	17.2%
Conifer Snowy/Coastal	41440	0.4%	73437	0.6%
Wooded tundra	360388	3.6%	6643	0.1%
Mangrove	-	-	-	-
Non-optimized areas	-	-	-	-
Water	1269485	12.6%	384728	3.4%
Total	10100736	100.0%	11463986	100.0%

Table 4: Ecosystem areas over the two TransCom regions covering North America.

Note on “Semitundra”: this is a potentially misleading shorthand abbreviation for a collection of ecosystems comprising semi-desert, shrubs, steppe, and polar+alpine tundra. The “Semitundra” zones appearing in northern Africa where one expects to find the Sahara desert are not, of course, tundra environments. They are instead semi-desert zones.

Transcom regions (<http://www.purdue.edu/transcom/>)

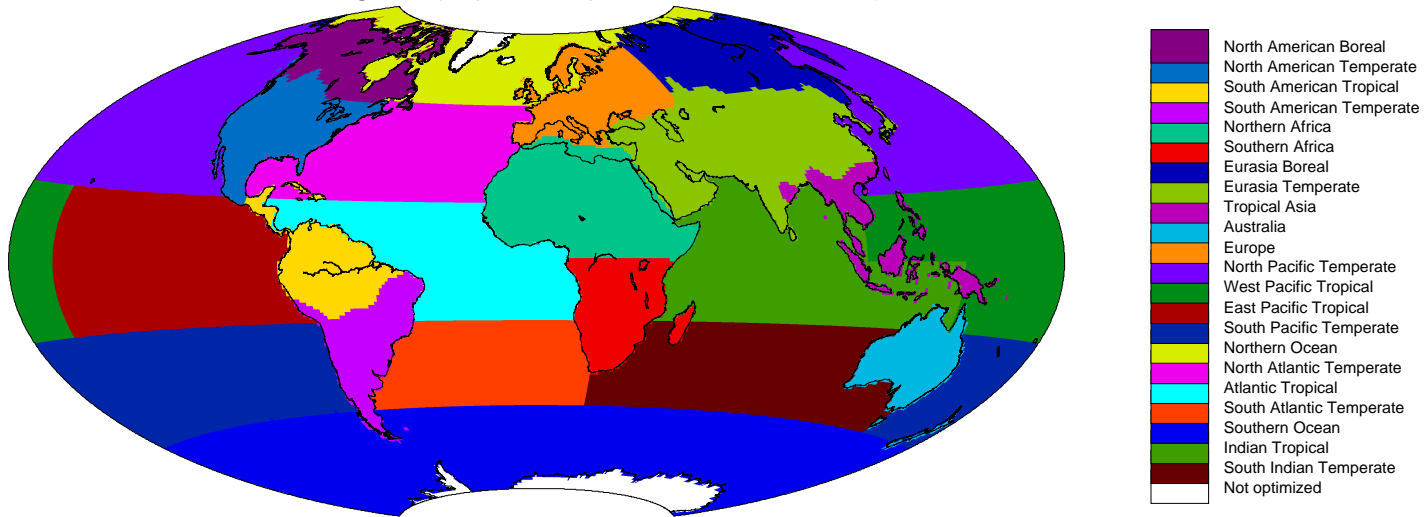


Figure 16: The 11 land regions and 11 ocean regions of the TransCom project

9.2 Why use ecoregions?

A fundamental challenge to atmospheric inversions like CarbonTracker is that there are not enough observations to directly constrain fluxes at all times and in all places. It is therefore necessary to find a way to reduce the number of unknowns being estimated. Strategies to reduce the number of unknowns in problems like this one generally impose information from external sources. In CarbonTracker, we reduce the problem size both by estimating fluxes at the ecoregion scale, and by using a terrestrial biological model to give a first guess flux from the ecoregion. The model is also used to give the spatial and temporal distribution of CO₂ flux within a region and week.

9.3 Ecosystems within TransCom regions

Each TransCom land region (Figure 16) can contain up to 19 ecoregions.

9.4 References

- [Olson ecosystem types](#)

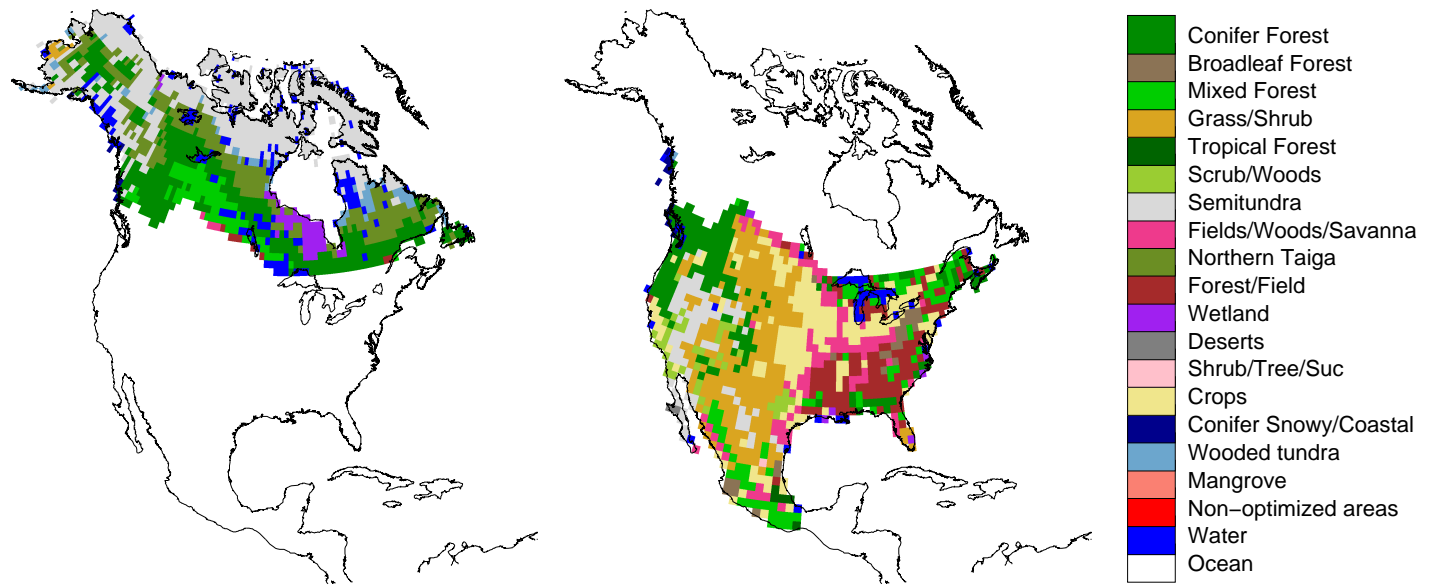


Figure 17: Ecoregions within the North American Boreal (left) and North American Temperate (right) TransCom regions.

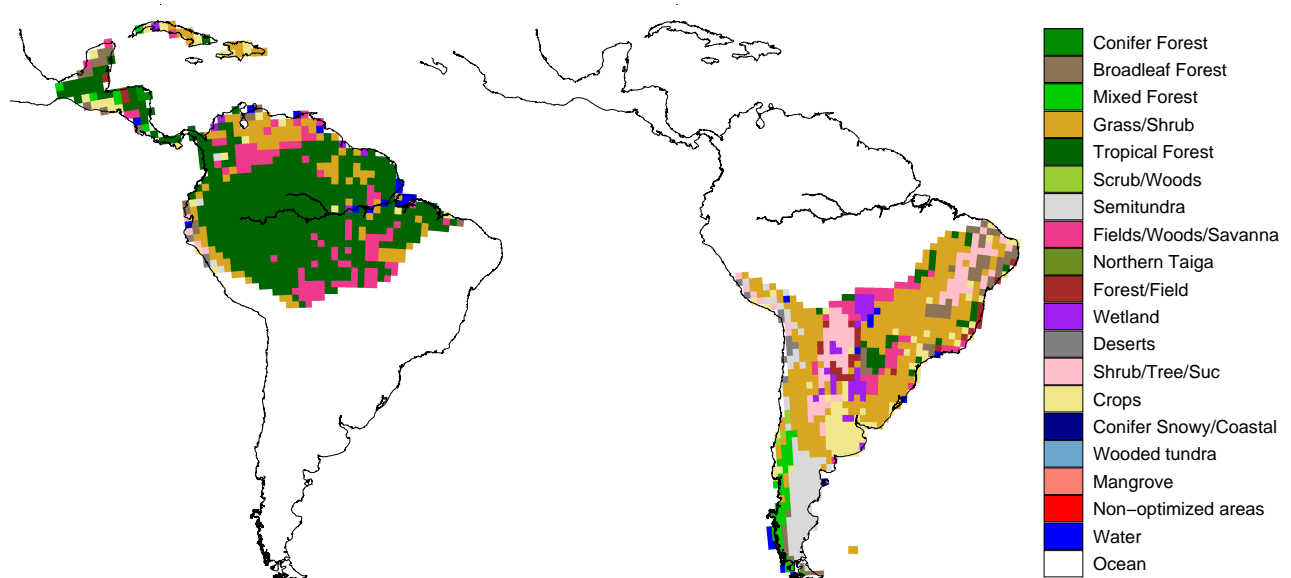


Figure 18: Ecoregions within the South American Tropical (left) and South American Temperate (right) TransCom regions.

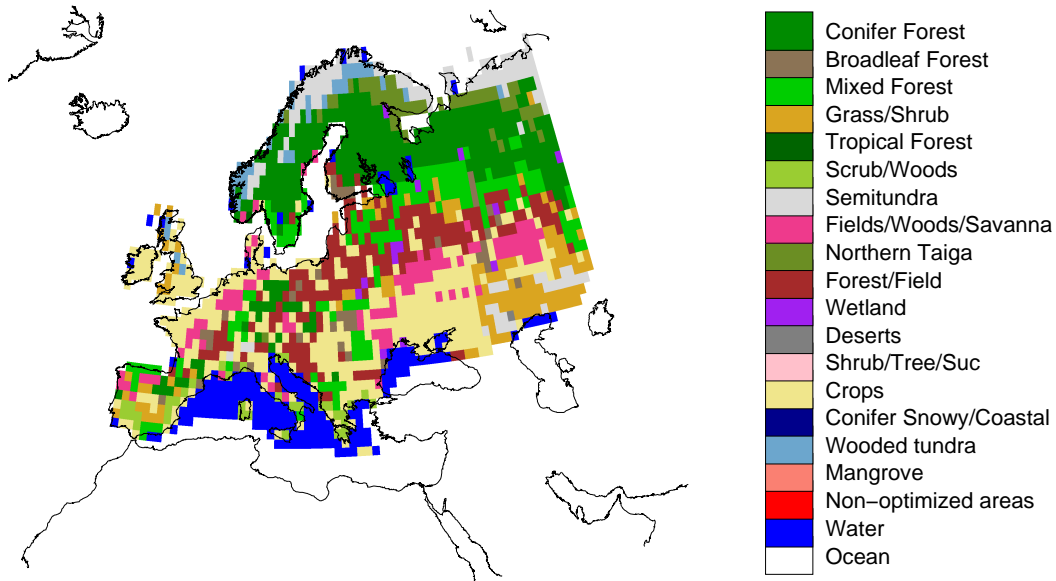


Figure 19: Ecoregions within the Europe TransCom region.

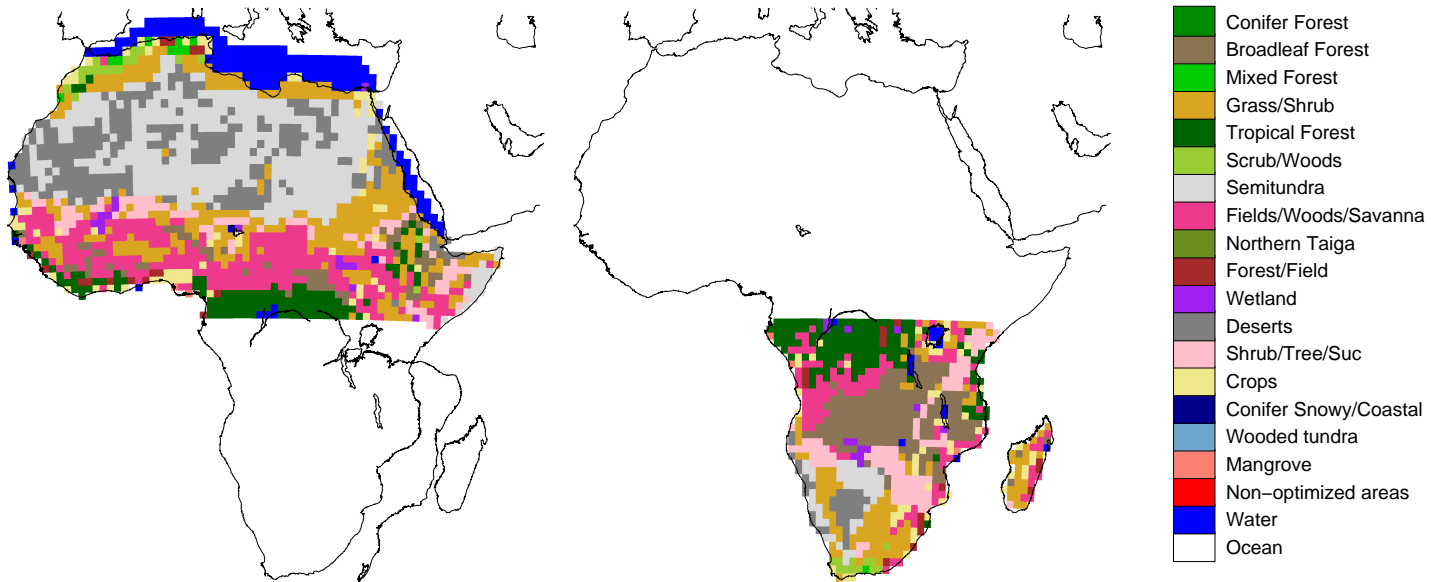


Figure 20: Ecoregions within the Northern Africa (left) and Southern Africa (right) TransCom regions.